Earth-Science Reviews 244 (2023) 104518

Contents lists available at ScienceDirect

Earth-Science Reviews

journal homepage: www.elsevier.com/locate/earscirev

Evaluating tomotectonic plate reconstructions using geodynamic models with data assimilation, the case for North America

Yanchong Li [a], Lijun Liu [a,b,*], Diandian Peng [a], Hao Dong [c,d], Sanzhong Li [c,d]

[a] Depart of Geology, University of Illinois at Urbana-Champaign, Urbana, IL, USA
[b] State Key Laboratory of Lithospheric Evolution, Institute of Geology and Geophysics, Chinese Academy of Sciences, Beijing, China
[c] Frontiers Science Center for Deep Ocean Multispheres and Earth System, Key Lab of Submarine Geosciences and Prospecting Techniques, MOE and College of Marine Geosciences, Ocean University of China, Qingdao 266100, China
[d] Laboratory for Marine Geology, Qingdao National Laboratory for Marine Science and Technology, Qingdao 266237, China

ARTICLE INFO

Keywords:
Plate reconstruction
Seismic tomography
Net lithospheric rotation
Mantle flow
Subducting slab
Paleotopography

ABSTRACT

Reconstructions of Earth's past surface kinematics are traditionally based on a combination of relative plate motions inferred mostly from preserved seafloor information and an assumed absolute reference frame using data from hotspots and/or true polar wander. Recently, plate reconstructions progressively introduced constraints from deep mantle structures like those imaged through seismic tomography. This additional information is utilized through either implicit or explicit fashion, where the lateral location of an imaged mantle slab represents that of its paleo-trench with the age of initial subduction estimated from geological proxies and slab depth. Here we quantitatively evaluated the geodynamic and tectonic implications of three recent global plate reconstructions (Müller et al., 2016, 2019; and Clennett et al., 2020) by focusing on subduction beneath North America. These reconstructions imply different amounts of trench retreat, plate motion and subduction zones, due to their varying dependence on the tomotectonic constraints. We simulated their respective subduction histories since 200 Ma using a sequential data-assimilation methodology. The resulting present-day slab structures based on these reconstructions show clearly diagnostic differences, among which the model based on Müller et al., 2016 best matches seismic tomography and Mesozoic paleotopography constraints within North America, supporting the tomography-implied differential lithosphere motion relative to the mantle. In contrast, modeled results based on the explicit tomotectonic reconstruction of Clennett et al., 2020 match both slab structure/evolution and associated paleotopographic constraints to the least. Consequently, the presented data-assimilation geodynamic modeling exercise, through reproducing the associated subduction history and continental tectonics, could quantify the tectonic implications of different plate reconstructions. We propose that further implementing this exercise through an iterative geodynamic-tomographic-tectonic workflow could serve to improve the tomotectonic reconstruction.

1. Introduction

Plate reconstructions represent a fundamental outcome of the theory of plate tectonics for understanding Earth's past evolution. In the traditional exercise, past plate motions are extracted from the currently preserved seafloor age, where relative movements among different plates could be derived through global plate circuits, under assumptions of symmetrical seafloor spreading along mid-ocean ridges and linear extrapolation of information for regions with unclear or missing data (e.g., Engebretson et al., 1985; Müller et al., 2008). The available data of seafloor age and associated tectonic markers can help to derive the history of relative plate motion to as far back as the Late Cretaceous, beyond which indirect constraints like continental geology and non-marine paleomagnetic data are needed (Seton et al., 2012; Torsvik et al., 2019; Müller et al., 2016, 2019). Derivation of absolute plate motions with respect to the hypothetically fixed deep mantle, which finalize the plate reconstructions, further requires a global reference frame that is usually based on the surface trajectories of deep-rooted hotspots (Müller et al., 1993; O'Neill et al., 2005) and/or true polar wander paths (Steinberger and Torsvik, 2008; Torsvik et al., 2008; van der Meer et al., 2010; Müller et al., 2016).

A natural question arises regarding the correctness of reconstructed

* Corresponding author at: Depart of Geology, University of Illinois at Urbana-Champaign, Urbana, IL, USA.
E-mail address: ljliu@illionis.edu (L. Liu).

https://doi.org/10.1016/j.earscirev.2023.104518
Received 23 October 2022; Received in revised form 18 June 2023; Accepted 24 July 2023
Available online 29 July 2023

plates that have by now disappeared due to subduction, a process that destroys past plate information. Some researchers then further integrated possible traces of subducted plates inside the deep mantle as imaged through seismic tomography into existing reconstruction models, with the aim of better estimating the past configuration of lost tectonic plates (e.g., Bunge and Grand, 2000). Such efforts started to gain popularity in recent years (van der Meer et al., 2012; Liu, 2012; Sigloch and Mihalynuk, 2013; Wu et al., 2016; Clennett et al., 2020) while the resolving power of global tomography steadily increased (Amaru, 2007; Li et al., 2008; Simmons et al., 2010; Ritsema et al., 2011; Sigloch, 2011; Obayashi et al., 2013; French and Romanowicz, 2014; van der Meer et al., 2018; Hosseini et al., 2020; Lei et al., 2020).

Here we term the tomography-assisted exercise as tomotectonic reconstruction. In practice, more and more recent plate reconstructions are affected by this concept, not only because of the rich information in seismic tomography, but also due to the increasing mutual-dependence and nested nature of different reconstruction models. In practice, such tomotectonic reconstruction usually involves two steps: First, define the geographical location of the paleo-trench by matching tectonic records along continental margins with the surface projection of the observed slabs in the deep mantle, usually with an implicit or explicit assumption that the subducted slabs sink largely vertically inside the mantle. Second, each slab segment tends to represent an individual subduction episode whose initial age of subduction follows that of the corresponding magmatic arcs or that estimated based on the current slab depth divided by an assumed slab sinking rate. As a result, the seismic images could provide additional details of the subduction history in the region that would otherwise have a simpler kinematic history based solely on extrapolating surface constraints; these additional details may include more episodes of subduction (van der Meer et al., 2012), different plate distributions and kinematics (Wu et al., 2016; Clennett et al., 2020), or net rotation of the entire lithosphere (van der Meer et al., 2010).

Inferences from seismic tomography can affect plate reconstruction from its global mantle reference frame to regional plate-scale features. Since paleomagnetic data mostly constrain the latitudinal position of past subduction, seismic tomography could be used to refine the paleolongitude. For example, van der Meer et al. (2010) interpreted a global east-west offset between the location of three subducted slabs and that of their corresponding paleo arcs as reflecting a temporally varying longitudinal rotation of the entire lithosphere relative to the deep mantle since 250 Ma, with the maximum shift being 18° since the Jurassic (~180 Ma). This longitudinal shift forms a so called net lithospheric rotation (NLR), the mean motion of global lithosphere with respect to the mantle reference frame (Fig. 1). Consequently, some recent reconstructions adopted this inference but with a reduced amount of ~10° longitudinal shift during the Mesozoic (e.g., Müller et al., 2016; Torsvik et al., 2019) by noting that the extreme value of 18° seems too large to explain observed hotspot tracks (Butterworth et al., 2014). Other reconstructions chose to minimize the NLR at most times (e.g., Müller et al., 2019). Yet, some of them still indirectly use information and models derived from seismic tomography models, like the use of crustal thickness profile and the model of Tethys Ocean that is based on seismic tomography (Hosseinpour et al., 2016) in Müller et al., 2019. Technically, all these models are tomotectonic reconstructions, since they were more or less influenced by the tomographic inferences as stated above. Their different amounts of adopted NLR (Figs. S1, S2) represent a key reason for their different trench locations over time (Fig. 1), a factor strongly affecting subduction dynamics and surface tectonics (Christensen, 1996; Mao and Zhong, 2018; Peng et al., 2021a). We call this indirect tomographic constraint through affecting features such as the reference frame of plate reconstruction to be *implicit*.

At regional scales, seismic tomography could also be used in an *explicit* fashion to revise existing plate reconstructions, with an example being the subduction history below North America (See Table 1.). By projecting fast mantle anomalies vertically onto the surface for intra-oceanic regions, tomotectonic reconstructions can result in significantly more complex subduction scenarios, such as those recently proposed for the northern and northeastern Pacific region during the late

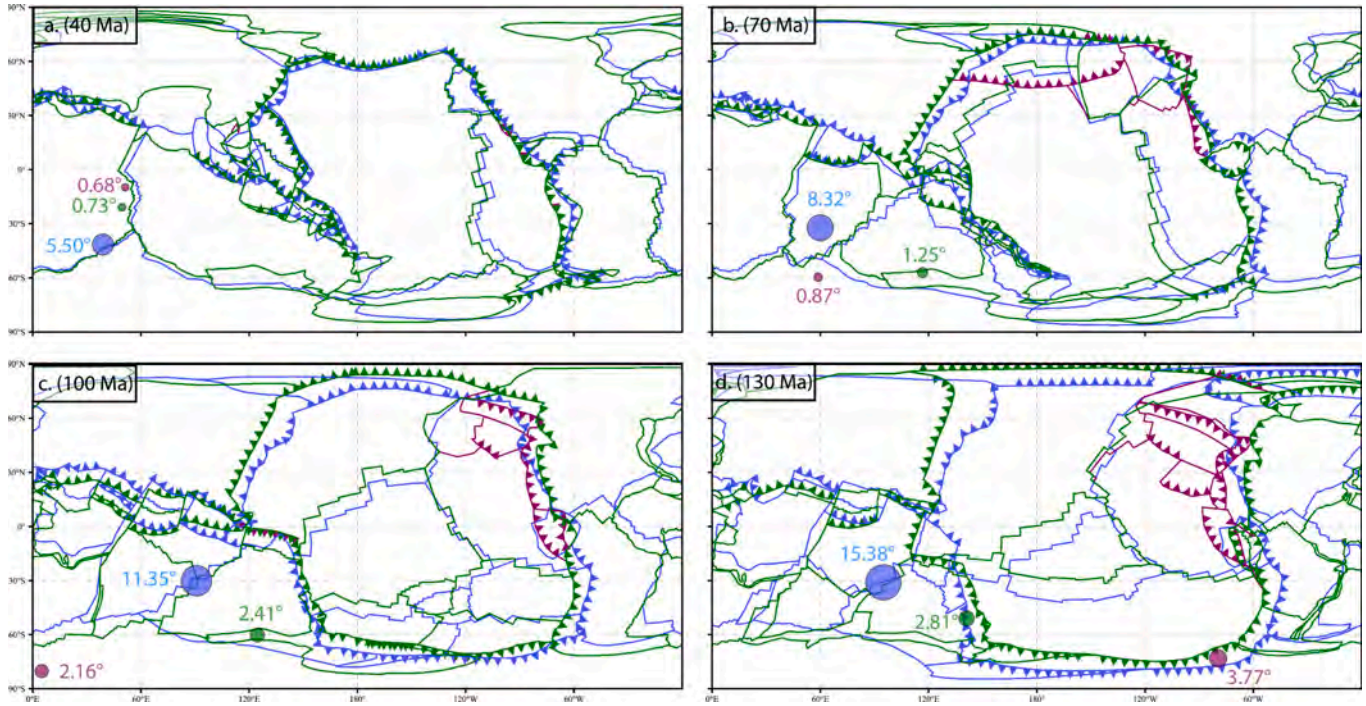

Fig. 1. Three recent global plate reconstructions at different times. Two of them (blue and green from Müller et al., 2016 and 2019, respectively) are based on the implicit tomotectonic reconstruction exercise, and the third one (purple from Clennett et al., 2020) represents an explicit tomotectonic reconstruction within the northeastern Pacific, with other regions following the reconstruction of Müller et al. (2019). The blue, green and purple dots mark Euler poles of accumulative net lithospheric rotation from respective time to 0 Ma from Müller et al., 2016 and 2019, and Clennett et al., 2020 respectively. The total displacements of net rotations are also shown in degrees. (For interpretation of the references to colour in this figure legend, the reader is referred to the web version of this article.)

Table 1
Mantle convection models based on different reconstructions.

Model name*	Reconstruction	Reference frame	NLR in 200 Ma	Tomotectonic features	Plate deformation
Mu16	Müller et al., 2016	Torsvik et al. (2008) (<70 Ma) van der Meer et al. (2010) (>70 Ma)	16.97°	Implicit, including NLR	No
Mu19	Müller et al., 2019	Minimized NLR together with trench migration velocity	2.59°	Implicit	Yes
Cl20	Clennett et al., 2020	Similar to Mu19	5.81°	Explicit for North America	Yes

* Every set of models comes with a SLM case and a WLM case, with lower mantle viscosity being 3×10^{22}Pas and 10^{23}Pas, respectively.

Mesozoic (Sigloch and Mihalynuk, 2013; Domeier et al., 2017), that were more recently assimilated into a global compilation (Clennett et al., 2020) based on the plate reconstruction of Müller et al. (2019). This reconstruction invokes multiple new oceanic plates west of the continental North America (Fig. 1), with much of its west coast (coinciding with the green line in Fig. 1) being a passive or transform margin until the latest Cretaceous (Fig. 1b). While some similar exercises from other groups concerning western and northern Pacific subduction seem to better match observation (Domeier et al., 2017; Lin et al., 2022), the recent reconstruction by Clennett et al. (2020), however, faces challenges from the uncertain terrane accretion processes along the margin (Coney et al., 1980; Burchfiel et al., 1992), enduring Mesozoic arc history (Clift et al., 2005; Pavlis et al., 2019), temporally varying stratigraphic records within the interior of continental North America (Heller and Liu, 2016; Li and Aschoff, 2022), and the implications on slab volume and trench stability (Coney and Reynolds, 1977; Saleeby, 2003; Liu and Zhou, 2015).

In this study, we attempt to evaluate the aforementioned global (implicit) and regional (explicit) effects of tomotectonic reconstructions using global-scale geodynamic simulations based on data assimilation. In doing so, the different plate reconstructions serve as surface boundary conditions to guide subduction at depths, where the modeled slabs can freely deform (shallowing, flattening, tearing, etc.) that may result in significant lateral slab displacement and segmentation (Peng and Liu, 2022). In particular, our tests hinge on the two underlying assumptions as mentioned above (vertical slab sinking and one-to-one correlation between slabs and subduction episodes) that went into these reconstructions. We choose to test three recent plate reconstructions that are related in some manner so their differences could be explicitly examined. The first two are from Müller et al. (2016) and Müller et al. (2019), respectively, where the former assumed rigid tectonic plates and latter further considers internal plate deformation. As demonstrated quantitatively (Fig. 1), these two reconstructions mainly differ in their global trench locations over time. Further decomposing these differences, we find that this mostly reflects their adopted different amounts of NLR (Figs. S1, S2), whose effect clearly dominates that due to deformable plate interiors which impact trench location only locally (comparing Figs. 1 and S2). The third reconstruction is based on an explicit tomotectonic compilation for the northeastern Pacific region during the late Mesozoic (Clennett et al., 2020), with other parts of the globe being identical to the reconstruction of Müller et al. (2019). Since the base reconstruction (Müller et al., 2019) assumes minimum NLR, in contrast to that implied in global tomography (van der Meer et al., 2010), the third reconstruction (Clennett et al., 2020) mostly incorporates regional tomographic constraints.

By assimilating the plate kinematic history including seafloor age, trench locations and plate motion of each reconstruction since 200 Ma into global forward mantle convection models, we first aim to reproduce their corresponding subduction histories and the resulting present-day slab structures inside the mantle. Based on model parameters such as viscosity chosen from our recent efforts in matching regional and global constraints (Hu et al., 2018a; Peng et al., 2021a, 2021b), we then examine the modeled subduction history, tectonic responses against surface geology, and the final mantle structures against seismic tomography for each plate reconstruction. In practice, we look for systematic differences among the examined reconstructions, as well as their capability in matching the available data constraints. Through this exercise, we hope to generate some new insight in the past plate kinematics on Earth, with a particular focus on the relationship between surface subduction history and slab evolution in the convective mantle. Given that the most significant difference among these three reconstructions concerns the subduction history below North America (Fig. 1), our effort will accordingly focus on this region.

2. Methodology

To effectively evaluate the tectonic and geodynamic implications of different plate reconstructions, we adopt a high-resolution global subduction simulator with sequential data assimilation (Liu and Stegman, 2011; Hu et al., 2016). The approach assimilates time-dependent information from plate reconstructions, including seafloor age, plate motion and plate boundary, into the geodynamic model, which starts integration at 200 Ma to avoid the effect of uncertain initial empty mantle on the predicted present day mantle structures. Data assimilation at every 1-Myr interval allows a seamless translation of past surface kinematics and evolving seafloor ages into subduction and mantle convection, while the resulting geodynamic history could make connections with geological records at the Earth's surface, as well as with the 3D mantle seismic structure at the present. Among recent efforts in reproducing a realistic Earth subduction history using the data-assimilation technique (Schuberth et al., 2009; Liu and Stegman, 2011; Steinberger et al., 2012; Bower et al., 2015; Zahirovic et al., 2016; Mao and Zhong, 2018; Hu et al., 2018a; Ma et al., 2019; Peng et al., 2021a, 2021b; 2022), our approach is unique in that it not only strictly satisfies the observed plate kinematics at the surface, but also produces natural-looking, tabular and asymmetric subducting slabs that could freely deform over time (e.g., Figs. 2, 9) below convergent boundaries (e.g., Liu and Stegman, 2011; Peng et al., 2021a, 2021b). Many of these important slab behaviors are absent in other time-dependent subduction models of data-assimilation due to the lack of proper representation of the sophisticated buoyancy and/or viscosity structures at subduction zones (Fig. 2) that are both challenging to implement and expensive (by >10 times than models without these features) to compute.

Another important difference between our data assimilation models and other recent exercises is that our dynamically evolving slabs and mantle flow allow more accurate calculation of the lithospheric deformation, especially during extreme events like flat slab subduction (Peng et al., 2021a; Liu et al., 2021). Consequently, this will allow reproduction of realistic surface topography and its variation over time, as due to not only the stress from the convective mantle (dynamic topography) but also buoyancy change within the lithosphere (isostatic topography). Consequently, our calculated surface topography (with ±8 km, Fig. 11) looks very earth-like, while previous studies usually present a much more subtle (with ±1 km) topography signal that is only reflecting dynamic topography.

The model implementation is based on the finite-element code CitcomS (Tan et al., 2006; Zhong et al., 2008). Since we focus on a relatively short geologic period (the last 200 Myr) of Earth's history, we approximate the convective mantle as an incompressible fluid that satisfies the Boussinesq approximation. The code solves the equations for

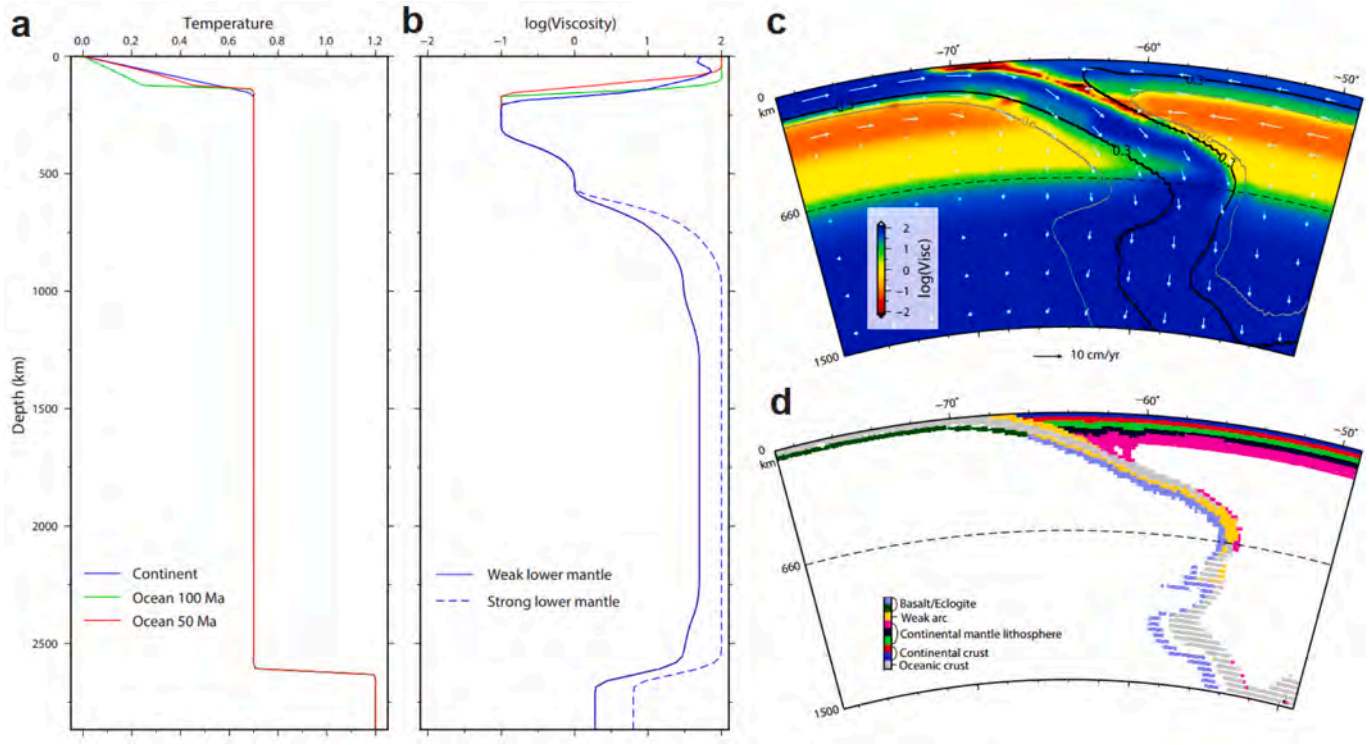

Fig. 2. Model temperature, viscosity, and composition. (a, b) Vertical profiles of initial temperature and viscosity for continental plates and oceanic plates with ages of 100 Ma and 50 Ma. Temperature is nondimensionalized relative to a reference value of 1000 °C. Viscosity is normalized by a reference viscosity of 10^{21} Pa·s. (c, d) Effective viscosity and composition of the Mu19 SLM model, with the illustration being a subduction zone along the western North America at 120 Ma. Isotherm of 0.6 and 0.3 are the grey and dark contours in c, respectively.

the conservation of mass, momentum, and energy, as well as the advection of chemical particles (tracers):

$$\nabla \bullet \vec{u} = 0, \tag{1}$$

$$-\nabla P + \nabla \bullet \left[\eta\left(\nabla \vec{u} + \nabla^T \vec{u}\right)\right] + \left(\rho_m \alpha \Delta T + \Delta \rho_c\right)\vec{g} = 0, \tag{2}$$

$$\frac{\partial T}{\partial t} + \vec{u} \bullet \nabla T = \kappa \nabla^2 T, \tag{3}$$

$$\frac{\partial C}{\partial t} + \vec{u} \bullet \nabla C = 0, \tag{4}$$

where $\vec{u}$ is the velocity, P is dynamic pressure, η is dynamic viscosity, ρ_m is the density of the ambient mantle, α is thermal expansion coefficient, ΔT is temperature anomaly, $\Delta\rho_c$ is compositional density anomaly, $\vec{g}$ is gravitational acceleration, and C is composition.

The global numerical mesh is divided into 12 spherical caps, each having 257 × 257 × 113 nodes in latitude×longitude×radius. This results in a resolution in the horizontal direction of ~23 km at the surface and ~ 12 km near the core-mantle boundary (CMB). We apply a radial mesh refinement such that the vertical resolution is ~ 12 km near the surface, ~ 26 km near the CMB, and ~ 31 km in the mid-mantle. This resolution is higher than that in most published models of its kind and allows a proper representation of the major thermal and compositional structures of the lithosphere, especially along plate boundaries. The initial temperature profile of oceanic plates follows a modified error-function (Liu and Stegman, 2011) with seafloor age adopted from the plate reconstruction (the resulting slab buoyancy is the same as that of the actual Earth), while continental plates have a steady-state initial temperature profile (Fig. 2a) and the temperature in CMB fixed. The viscosity structure depends on depth, temperature, and composition, with a layered background viscosity profile and a reference viscosity of 10^{21} Pas (Fig. 2b, c). The viscosity is calculated as:

$$\eta = \eta_0(r) \cdot C \cdot exp\left(\frac{E_\eta(r)}{T + T_\eta(r)} - \frac{E_\eta(r)}{T_m + T_\eta(r)}\right) \tag{5}$$

where η is the effective viscosity, $\eta_0(r)$ is the depth-dependent background viscosity (Fig. 2b), C is the compositional multiplier (see Table S1), $E_\eta(r)$ is the activation energy, $T_\eta(r)$ is the activation temperature (see Table S2), T is temperature and T_m is the ambient mantle temperature. The base of the mantle is free to slip while the surface assimilates velocities from plate reconstructions (Müller et al., 2016, 2019; Clennett et al., 2020).

A total of ~1.8 billion tracers, each with thirteen flavors, are used to define and track the composition, migration, and deformation of different model components. The continental lithosphere consists of a 2-layer crust and 3-layer mantle lithosphere (Fig. 2d). The crust has an average density of ~2.8 g/cm^3, where the lower crust is weaker than the upper crust, as helps to minimize the effect of imposed surface kinematics on lithospheric deformation at depth. The mantle lithosphere has a chemically buoyant upper layer, a neutrally buoyant middle layer, and a dense lower layer, all relative to the ambient mantle, following our recent inference on the lithospheric density profile below continents (Hu et al., 2018b; Wang et al., 2022a, 2022b). The oceanic plate consists of three compositions: a 7-km-thick surface layer that has no buoyancy anomaly but mimics the viscosity effect of a weak and lubricating plate interface near the trenches during subduction (Fig. 2c), a basaltic crustal layer below the weak surface layer, and the underlying lithospheric mantle (Fig. 2d). When the chemically buoyant oceanic crust subducted to 120 km or deeper, its composition and density change following the basalt-to-eclogite phase transformation (Fig. 2d). This buoyancy setup results in realistic-looking Earth topography both in the past and the present day (section 3.2.3). See Table S1 for a complete set of composition density profile. The effect of background mantle viscosity profile has been extensively tested in our previous studies with both regional (Liu and Stegman, 2011; Hu et al., 2016; Zhou et al., 2018) and global

simulations (Hu et al., 2018a; Peng et al., 2021a, 2021b). In this study, we present results from two global models with different lower-mantle viscosity values, to indicate this effect.

The above adopted model parameters generate an Earth-like convection vigor. For example, the resulting sinking rate of the slab at upper-mantle depth is similar as the observed plate velocities (Fig. 2c), and this remains largely unchanged when the surface is set to be free-slip, a process for explicitly testing the dynamic compatibility of the convective mantle and surface plates (Liu et al., 2022). The effective viscosity across the subduction zone determines the model's capability in reproducing real Earth dynamic processes. In our model, this varies by four orders of magnitude, ranging from a very weak ($\sim 10^{19}$ Pa s) plate interface to a weak ($\sim 10^{20}$ Pa s) asthenosphere, to a strong ($\sim 10^{22}$ Pa s) slab hinge, and to very strong ($\sim 10^{23}$ Pa s) lithosphere and slabs further away (Fig. 2c), consistent with studies of free subduction (e.g., Stadler et al., 2010; Gerya et al., 2021). The compositional evolution of the model is also reasonable, where the different tracer types help to track the geometry and deformation of subducting slabs, continental lithosphere, as well as other model components (Fig. 2d).

In this study, we attempt multiple approaches to evaluate the different plate reconstructions. These include a systematic comparison of the modeled slab structures with seismic tomography, where we considered GyPSum-S (Simmons et al., 2010), GLAD-M25 (Lei et al., 2020), UUP-07 (Amaru, 2007), and DETOX-P3 (Hosseini et al., 2020). This is realized through generating both intuitive 3D images and quantitative correlations along cross sections focusing on North America. For the correlation exercise, we first compute the fraction of modeled slabs within the whole cross sectional area at each depth by tracking the temperature of >50 °C colder than the ambient mantle, and then match it with the fast seismic anomalies in tomography (> 0.4% for S-wave velocity or > 0.2% for P-wave velocity for proper visual comparison); the value of fitting is 1 when the cold slab fully overlaps the tomographic slab, and is 0 when they are entirely off or there is no slab in the region of investigation.

Another important approach for how we evaluate the different plate reconstructions is through examining their corresponding temporal subduction evolution and comparing the associated surface topographic histories (see section 3.2.3 for more details) with available geological records. In our focused study region of North America, we first examine the temporal variation of slab dip angle, where a prominent latest Cretaceous – early Cenozoic flat Farallon slab was well inferred from tectonic data (Coney and Reynolds, 1977; Saleeby, 2003; DeCelles, 2004; Liu and Gurnis, 2010; Liu et al., 2011). We then examine the associated surface topographic predictions from different models, with a particular focus on the dramatic paleo-elevation changes since the Jurassic time, including dominantly subaerial topography of western U. S. prior to the mid-Cretaceous with prominent Early-Cretaceous regional downward dipping (Heller et al., 2003; Heller and Liu, 2016), formation of the widespread Late-Cretaceous Western Interior Seaway (Bond, 1976; DeCelles, 2004; Liu et al., 2008), and the present-day east-west topographic dichotomy.

3. Data-assimilation modeling results based on different reconstructions

We present the numerical results from three sets of data-assimilation models (Mu16, Mu19, and Cl20) based on the three respective plate reconstructions (Müller et al., 2016, 2019; Clennett et al., 2020). Among them, the results of Mu16 have been previously evaluated against geological and geophysical data in East Asia both during the Mesozoic (Peng et al., 2021a) and at the present (Peng et al., 2021b). For all three sets of models, we adopt two different background mantle viscosity profiles (Fig. 2b) with the main difference being the lower-mantle viscosity that affects slab evolution (depth and lateral location) the most (e.g., Liu and Gurnis, 2008; Spasojević et al., 2009; Peng and Liu, 2022). Intuitively, a strong lower mantle (SLM) leads to shallower present-day slabs than with a weak lower mantle (WLM). In our simulations, the SLM case has a viscosity 3-times of that in the WLM case. With this viscosity range, Mu16 produces global slabs whose present depth and location largely match those revealed in seismic tomography (Peng and Liu, 2022). Here, we further apply this viscosity range to Mu19 and Cl20, to investigate the possible slab behaviors due to this plausible mantle viscosity variation.

In the following sections, we thoroughly analyze these simulation results, both for the present day and the geological past. In section 3.1, we evaluate the implicit implication of tomography on global plate motions (e.g., van der Meer et al., 2010) by comparing the present-day slab structures across four major subduction zones from two numerical models (Mu16 and Mu19) that have contrasting amounts of NLR. In section 3.2, we further examine this implicit tomographic constraint (NLR) while also evaluate the explicitly revised regional reconstruction based on tomographic features below North America through comparing three model results (Mu16, Mu19 and Cl20) with observations. In this section, we first focus on their differences in modeled present slab structures due to discrepancies among their adopted plate reconstructions. Second, we analyze their corresponding subduction evolution below North America since the Mesozoic. Finally, we evaluate their associated surface topographic expressions by comparing with the Mesozoic stratigraphic records from west-central North America.

3.1. Effects of tomography-derived net lithospheric rotation on global slab evolution

The three adopted plate reconstructions utilize two base reference frames (Fig. 1), one with large amplitudes of net lithospheric rotation (Müller et al., 2016), and the other with much reduced net rotation (Müller et al., 2019). This difference causes lateral offsets (~1000 km) of past trench locations since the Mesozoic that are much larger than those due to internal deformation (~100 km) of continents for most places. In the reconstruction of Müller et al. (2019), these two effects combine to generate trench offsets that influence the evolution of subducting slabs globally. To minimize the dynamic effect of toroidal flow and deformation close to slab edges (Schellart et al., 2007; Liu and Stegman, 2011), we choose to examine slab structures at the interior of four major subduction zones: East Asia, South Asia, North America, and South America (Fig. 3).

Overall, we observe a good match between the present-day slab structures from the two subduction models and the fast anomalies from seismic tomography (Fig. 3, UUP-07 from Amaru, 2007). A similar match with other tomography images for model Mu16 was published earlier (Peng et al., 2021a; Peng and Liu, 2022). The generally good match at all four subduction zones confirms that these fast anomalies represent subducted slabs. Relatively speaking, the results in Mu16 provide a statistically better fit to tomography than those in Mu19 (Figs. 6, 7 and 8). Specifically, their quality of match seems similar in East Asia and South Asia, but Mu16 is notably better in North America and South America (Fig. 3c and d). Given that the modeled slab below North America in Mu19 is consistently shallower than that in tomography, we performed another model where we lower the mantle viscosity (WLM) so that this slab could sink deeper, a result that will be discussed in the next section. This vertical misfit, however, has little impact on the lateral location of slabs, the purpose of this section.

In practice, the difference between these two reconstructions (Müller et al., 2016, 2019) implies different amounts of trench retreat (or advance) at locations along the path of net lithospheric rotation, such as East Asia, South America, and northern North America (Figs. 1 and S2). Since trench retreat has been a common mechanism for explaining lateral displacement of subducted slabs relative to their present-day trench (e.g., Christensen, 1996; Mao and Zhong, 2018), a comparison of model results from Mu16 and Mu19 allows us to further evaluate this mechanism using real Earth data. This intuition is confirmed with the model results in that subducted slabs along retreating trenches are now

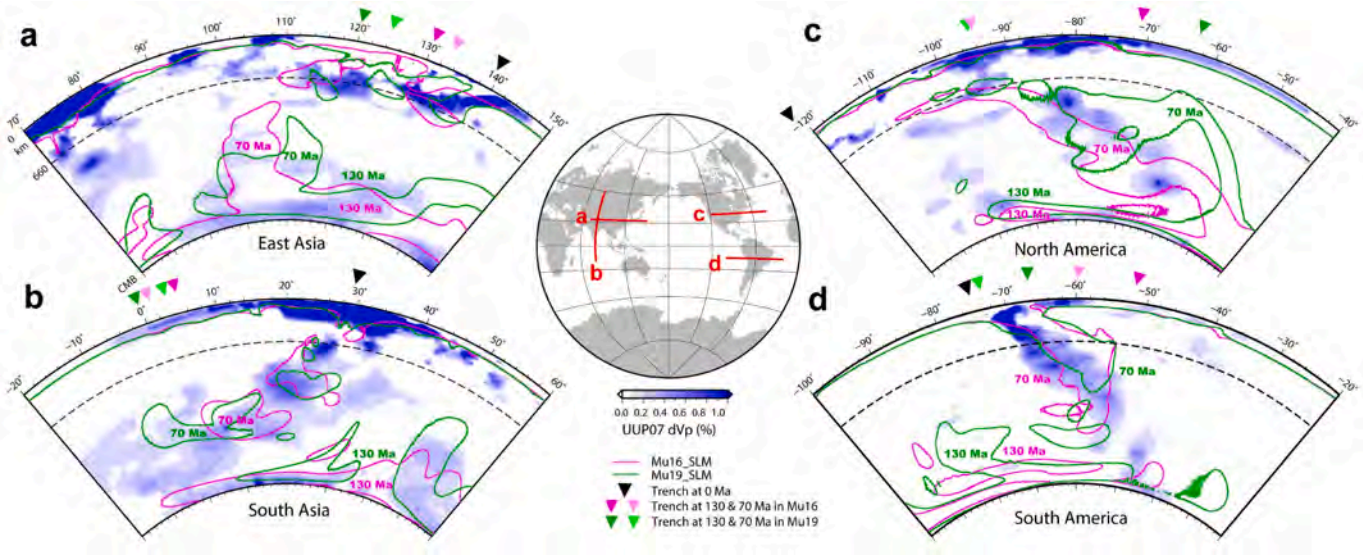

Fig. 3. Modeled present slab structures at four major subduction zones. Cross sectional comparison of modeled versus observed slab geometry in present-day along a) East Asia, b) South Asia, c) North America, and d) South America. The magenta and green slab contours (100 °C colder than the ambient mantle) correspond to results from Mu16 and Mu19, both with a strong lower mantle (SLM). The reversed triangles mark the locations of the trench at 130 Ma, 70 Ma, and the present from different reconstructions. Ages in the mantle mark the time of subduction for the nearby slab portion. Note the overall similar lateral locations of subducted slabs from the two models as well as relative to those in tomography. (For interpretation of the references to colour in this figure legend, the reader is referred to the web version of this article.)

located far below the overriding plate (Fig. 3a,c,d), while the slab along an advancing trench is below the subducting plate (Fig. 3b).

Then we more quantitatively analyze these results. Assuming slabs sink largely vertically after their initial subduction (as also commonly presumed in tomotectonic reconstructions), the present geographic location of slabs should be roughly the same as that of the paleo trench. In other words, the amount of trench retreat since initial subduction should largely equal to the lateral displacement between the subducted slab and the present-day trench. However, with a close examination of these model results, the above intuitive interpretation clearly fails along most subduction zones. For example, although the paleo-trench locations vary significantly (by >1000 km since the Mesozoic) among the two plate reconstructions (Figs. 1, 3), the lateral location and displacement of their slabs relative to the present trenches are very similar, instead of being proportional to the amounts of trench retreat they experienced as suggested in regional subduction models (e.g., Christensen, 1996). According to recent global geodynamic simulations (Steinberger et al., 2012; Peng and Liu, 2022) and tomographic-tectonic correlation analysis (Domeier et al., 2016), Mesozoic subduction usually correlates with the lower-mantle slabs at the present, with slabs subducted prior to ~130 Ma mostly piling up above the CMB. Indeed, the lateral positions (measured at both the center and edges) of the lowermost mantle slabs based on the two reconstructions are nearly identical below all four subduction zones (Fig. 3), although their associated amount of trench retreat could differ by a factor of 2 (e.g., Fig. 3a,d). This means that the lateral slab migration within the mantle is not solely driven by the imposed NLR, but rather likely stems out from the internal dynamics of the convective mantle.

At mid-mantle depths, the observed relationship between slab location and paleo-trench position is equally puzzling. We find that, except in South Asia where the neoTethyan slab subducted via dominant trench advance, the mid-mantle slabs in all other regions are located significantly more (by a factor of 2) landward than implied by their corresponding trench locations (e.g., at ~70 Ma) (Fig. 3). This indicates that slabs along a retreating trench usually do not sink vertically, but instead travel progressively inland while descending. For example, in North America, the distance the subducting slab has traveled horizontally since 70 Ma is greater than (Mu19) or close to (Mu16) that in the vertical direction. Therefore, we conclude that the present slab location cannot represent that of the paleo trenches, and that doing so in plate reconstructions would result in significantly different (usually older) ages of past subduction compared to the real scenario. In the case of North America, the current exercise of tomotectonic reconstruction would convert the present location of the 70-Ma slab in Mu19 and Mu16 to an apparent subduction age of 130 Ma and 120 Ma, respectively.

Not only the amount of trench retreat does not equal to that of slab lateral displacement, but also even the polarity of past trenches may be mistakenly inferred from the present seismic slab distribution. For example, in East Asia, the more westward trench location at 70 Ma in Mu19 generates mid-mantle slabs that are more eastward relative to Mu16 (Fig. 3a). Similarly in South America, some Mesozoic slabs are below the ocean and west of the continent (Fig. 3d). This oceanward translation of the subducted slab would imply intra-oceanic subduction in the past, according to the current tomotectonic assumption. All the above surprising observations challenge the common hypothesis of trench retreat as a key control for subducted slab locations and the commonly adopted assumption of vertically sinking slabs inside the mantle in recent tomotectonic reconstructions.

3.2. *Evaluating implicit and explicit tomotectonic inferences in North America*

The general consistency of modeled slab structures in Mu16 and Mu19 with seismic tomography along all major subduction zones (Fig. 3) provides a basis for further evaluating the differences between the implicit and explicit tomotectonic reconstructions. For this purpose, we will focus on North America, due to the availability of both such reconstructions and the high-quality tomographic and geological constraints in the region. Below, we will systematically evaluate the present slab structures, their temporal evolution, as well as the associated paleotopography predictions.

3.2.1. *Present-day slab structures*

For comparison with the different numerical model results, we utilize a recent tomography model GLAD-M25 that is based on full-waveform tomography and the seismic data from USArray (Lei et al., 2020). This

tomography result outlines a similar configuration of the major fast anomalies below North America as in most previous tomographic inversions, but its resolved structures are more coherent and with more prominent seismic velocity perturbations. We start with an evaluation of the map-view consistency between modeled slabs and major fast seismic anomalies (i.e., seismic slabs) below North America (Fig. 4). These seismic anomalies are traditionally interpreted to be the subducted Farallon slab. Recently, Sigloch and Mihalynuk (2013) proposed that they represent slab piles due to intra-oceanic subduction west of continental North America.

Here we present three sets of subduction models: Mu16, Mu19, and Cl20, each with two different mantle viscosity profiles (SLM & WLM, Fig. 2b). To cover the slabs subducted from the late Mesozoic (~200 Ma) to the early Cenozoic (~50 Ma), the period when the three plate reconstructions differ the most (Fig. 1, Movie S1), we choose five different depths within the lower mantle. At 700–1000 km depths, the

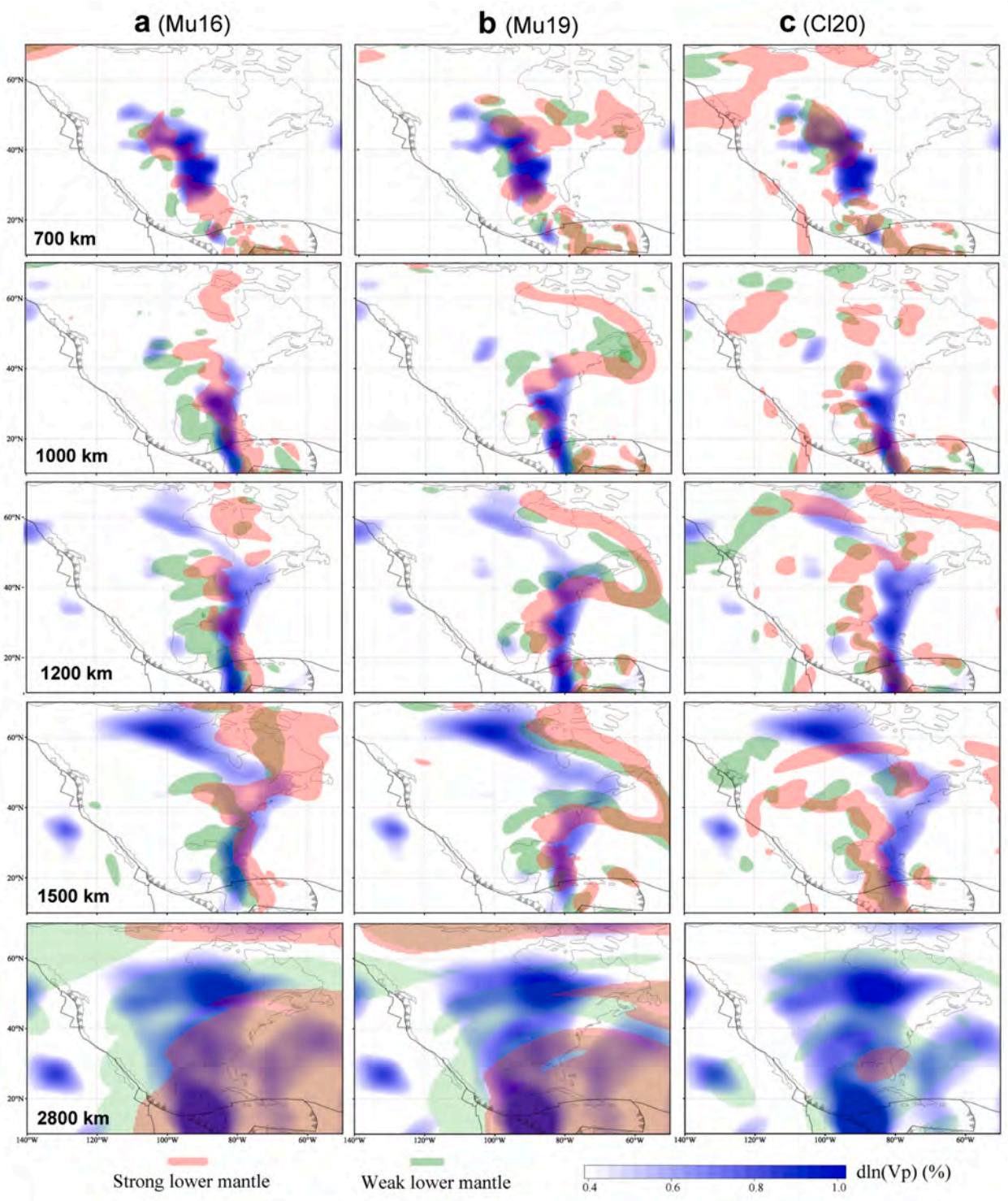

Fig. 4. Comparison of three subduction models with GLAD-M25. Each row represents a different depth and each column a different reconstruction, all with modeled slabs (200 °C and colder than the ambient mantle) overplotted on the seismic image. For each plate reconstruction, we performed two subduction models with a strong and weak lower mantle.

tomography reveals a localized slab, mostly below central-eastern United States. All subduction models generate this slab, although to different extents. Mu16, which most closely reproduces this structure, suggests this represents the subducted Farallon plate. In contrast, Mu19 (Fig. 4b) and Cl20 (Fig. 4c) only predict part of this structure but with additional large volumes of slab further east and north, where there are no seismic counterparts. A weaker mantle viscosity leads to a similar distribution of slabs for each model. This contrast among the three models is more clearly shown in the 3D visualization (Fig. 5) where the slabs in Mu19 and Cl20 are more widespread at shallow (<700 km) depths.

At middle mantle (1200–1500 km) depths, the spatial distribution of the seismic slab extends further north into Canada. All numerical models show the same spatial trend as well. However, these model results display systematic discrepancies in the *E*-W direction. To the south of 50°N, Mu16 best matches the overall location of the seismic slab, but Mu19 and Cl20 demonstrate progressive westward offset from the tomography. North of this latitude, the mismatch largely goes the opposite way with all three models predicting slabs too far to the east. Among them, Cl20 also predicts multiple sub-parallel slab branches due to the multiple trenches going into this reconstruction (Fig. 1). Although one of these slabs partly overlaps the single seismic slab below western Hudson Bay, the other slabs do not match any prominent seismic anomalies. At 1500 km depth, Cl20 demonstrates the most significant deviations from tomography, where its largest slab system is systematically too to the west and south of the observed slab. Near the CMB where the oldest slabs

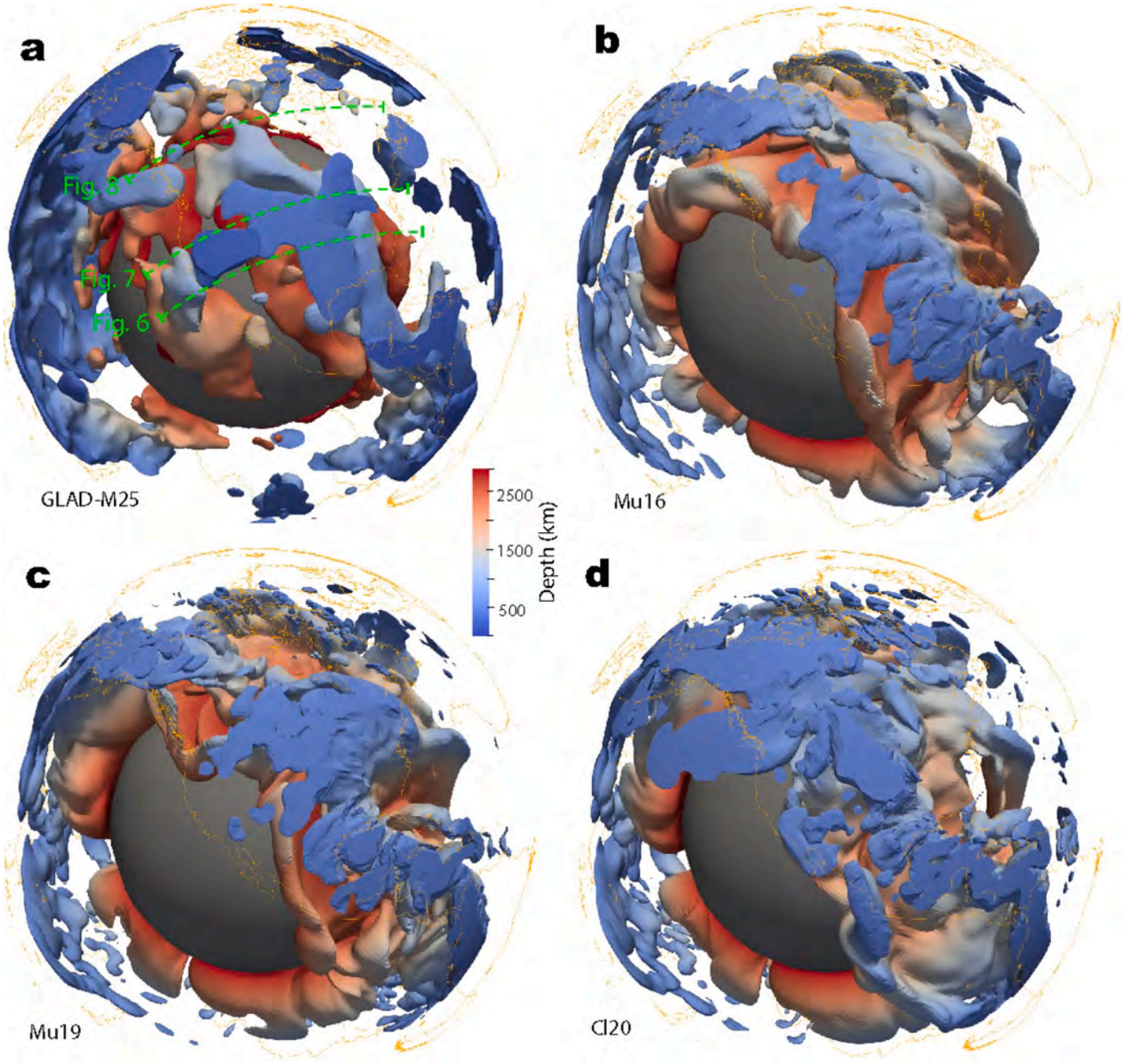

Fig. 5. 3D visualization of observed and predicted slabs below North America. a) Seismic topography GLAD-M25. Green dashed lines mark profile locations of Figs. 6-8. b-d) Present-day slabs from Mu16_SLM, Mu19_SLM, and Cl20_SLM, respectively. Mantle structures below 500 km depth are shown. Slab surfaces correspond to the −100 °C isotherm, with colour showing slab depth for all panels. (For interpretation of the references to colour in this figure legend, the reader is referred to the web version of this article.)

reside, all three models could capture at least part of the seismic slabs. Relatively speaking, Cl20 predicts the smallest volume of slabs at this depth, while Mu16 reproduces the most.

For a more quantitative comparison, we further examine the slab structures along three E-W cross sections along 30°N (Fig. 6), 40°N (Fig. 7), and 60°N (Fig. 8), whose surface locations are shown in Fig. 5a. Among these profiles, 40°N represents a common location for examining the Farallon slab, while the other two profiles further south and north respectively sample two 'outboard' slabs in the eastern and northern Pacific that are recently interpreted as recording Mesozoic intra-oceanic subduction (Sigloch and Mihalynuk, 2013; Domeier et al., 2017). To evaluate the robustness of the relevant seismic features, we also consider two other seismic tomography images: GyPSuM-S (Simmons et al., 2010) and DETOX-P3 (Hosseini et al., 2020), both with good data coverage for the study area.

Along 30°N, all three tomography images reveal a prominent coherent seismic slab traditionally regarded the Farallon slab that extends from ~700 km depth at −90°E to nearly the CMB below −70°E. Results from Mu16, Mu19, and Cl20 all show this major slab, especially the SLM models, where that from Mu16 provides the closest match. We also observe a successive steepening and westward shift in slab location from the first (Mu16) to the third (Cl20) model. These tomography images also resolve some secondary fast anomalies west of the main Farallon slab, but both the geometry and location of this feature remain unclear based on these images. Among the three subduction models, Cl20 produces a most prominent secondary slab, but its location is shifted westward by >500 km relative to DETOX-P3, based on which the reconstruction was built (Clennett et al., 2020). Consequently, the quantitative fit of model with tomography along this profile is consistently the highest for Mu16 at most depths and lowest for Cl20 (Fig. 6c), mostly due to offsets in location and shape of the latter. It is worth noting that a weak lower mantle (WLM) consistently degrades the model fitting at this latitude (green contours in Fig. 6).

The comparison of modeled versus observed slabs along 40°N is similar as that along 30°N, but with the Farallon slab in Mu19 being significantly shallower than in the other two models. The WLM case worsens for all other models. In a map view, the shallow Mu19 slab (Fig. 7b) represents a sharp eastward extrusion of the flat Farallon slab at this latitude (Fig. 5b). As shown later (section 3.3), this feature is a result of an enormous Mesozoic flat slab driven by the fast trench retreat required in the plate reconstruction (Figs. 1,3c). This abnormal slab behavior also caused excessive Mesozoic subsidence of the North American continent (section 3.2.3). These observations help to quantify the amount of net lithospheric rotation in reconstructing absolute plate motions. Another observation is that the Cl20 model predicts an excessive volume of slabs that are also too deep and further west compared to tomography. Again, the quantitative match with tomography at each depth is the highest for Mu16, and lowest for Cl20, due to reasons analyzed above for 30°N.

Further north at 60°N, the observed slab structure becomes notably different: the broad fast anomaly implies the slab is more *E*-W oriented than in the south (Fig. 7a), consistent with the counter-clockwise bending of the Farallon slab (Figs. 4,5). Both Mu16 and Mu19 predict the slab whose location is too to the east, although their slab volume seems appropriate (Fig. 7b). In contrast, Cl20 seems to better reproduce the lateral location of the seismic slabs, although the modeled slabs are too shallow compared to tomography. This is one branch of several slabs originated from multiple intra-oceanic subduction zones (Fig. 4c) in this reconstruction (Fig. 1; Clennett et al., 2020). Consequently, the quantitative match for Cl20 at depths <1500 km becomes similar as or slightly higher than for Mu16 and Mu19, but its match in the deeper mantle remains the poorest (Fig. 7c). The WLM counterparts of these results only make the fit even worse.

Collectively, the analyses in this section suggest that among the three different reconstructions, the one (Mu16) that allows large net lithosphere rotation produces slab structure most consistent with mantle seismic images. Furthermore, subduction models (Mu16 & Mu19) based on the implicit tomotectonic reconstructions (Müller et al., 2016, 2019) can better match the mantle seismic structure below North America than that (Cl20) based on the explicit tomotectonic reconstruction (Clennett

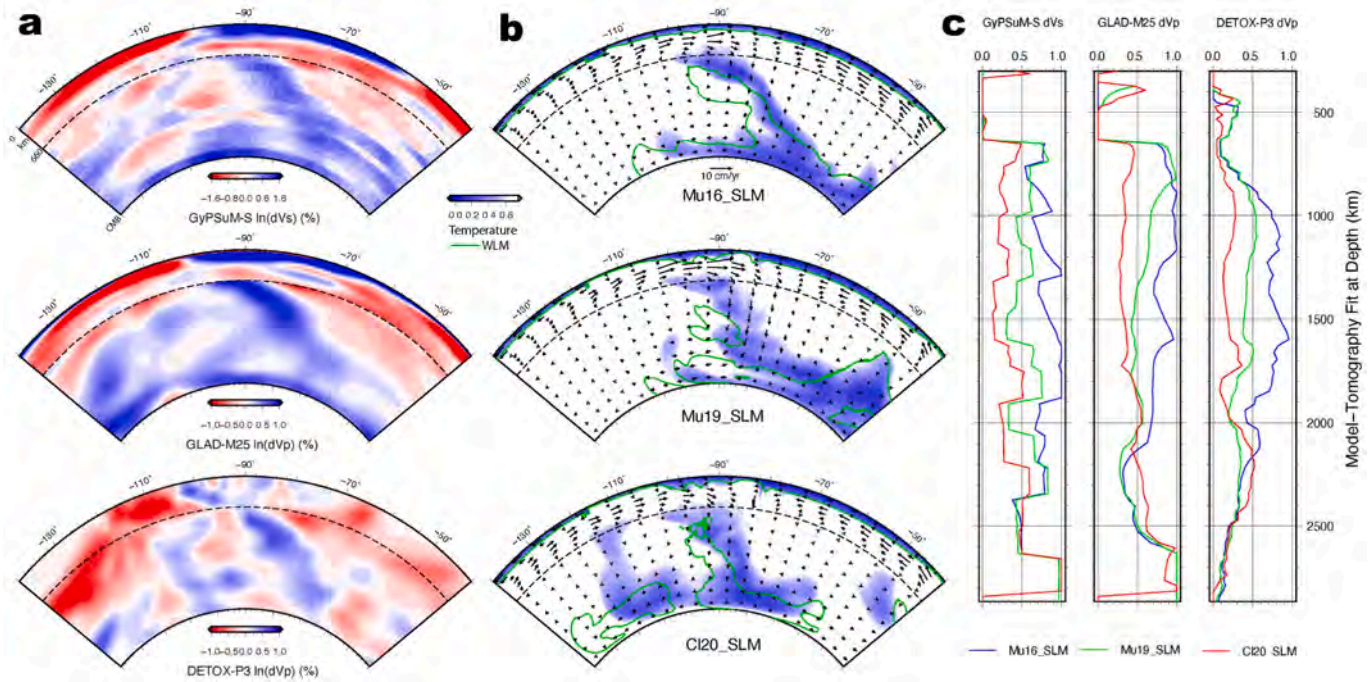

Fig. 6. Comparison of seismic tomography with modeled slab structures along 30°N. a) Seismic tomography from GyPSuM-S (Simmons et al., 2010), GLAD-M25 (Lei et al., 2020), and DETOX-P3 (Hosseini et al., 2020). b) The background colour represents predicted slab structures from Mu16_SLM, Mu19_SLM, and Cl20_SLM, while the green contours outline the slabs from their respective WLM cases. c) Quantitative match between the three modeled slabs and the three tomography images at each depth. (For interpretation of the references to colour in this figure legend, the reader is referred to the web version of this article.)

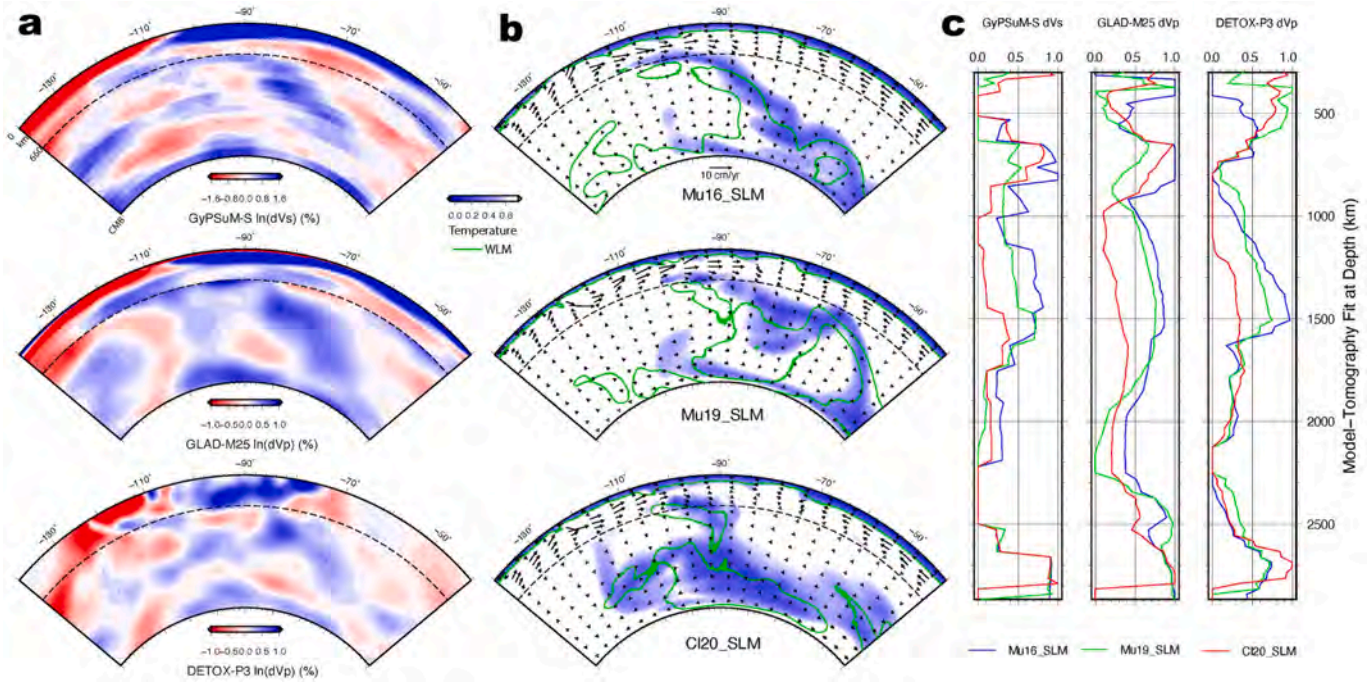

Fig. 7. Same as Fig. 6, but along 40°N.

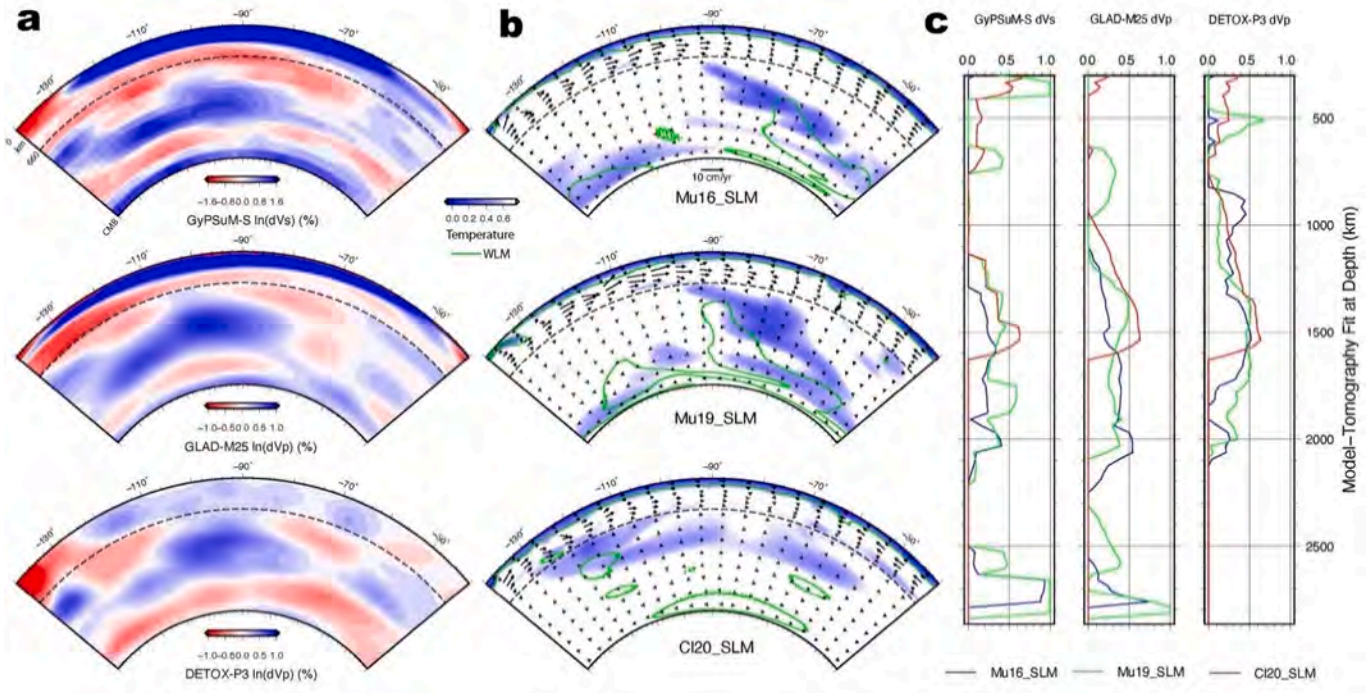

Fig. 8. Same as Fig. 6, but along 60°N.

et al., 2020), supporting that the dominant slab should represent the subducted Farallon plate. However, the secondary fast seismic anomalies west of the main Farallon slab suggest there is a need for Mesozoic intra-oceanic subduction within the northern and northeastern Pacific Ocean as the tomotectonic reconstruction argued for, although the resulting slab geometry and location based on the current reconstruction are still consistently off from observation.

3.2.2. Subduction history based on different plate reconstructions

A better understanding on the differences in the present-day slab structures based on the three plate reconstructions can be inferred from their respective evolution following the subduction history. We demonstrate the subduction history both along a vertical cross section at 40°N (Fig. 9), the center of the slab or slab pile, and through examining their corresponding 3D evolution (Fig. 10).

Based on the two implicit tomotectonic reconstructions, Mu16 and M19 both produce eastward Farallon subduction since the Jurassic.

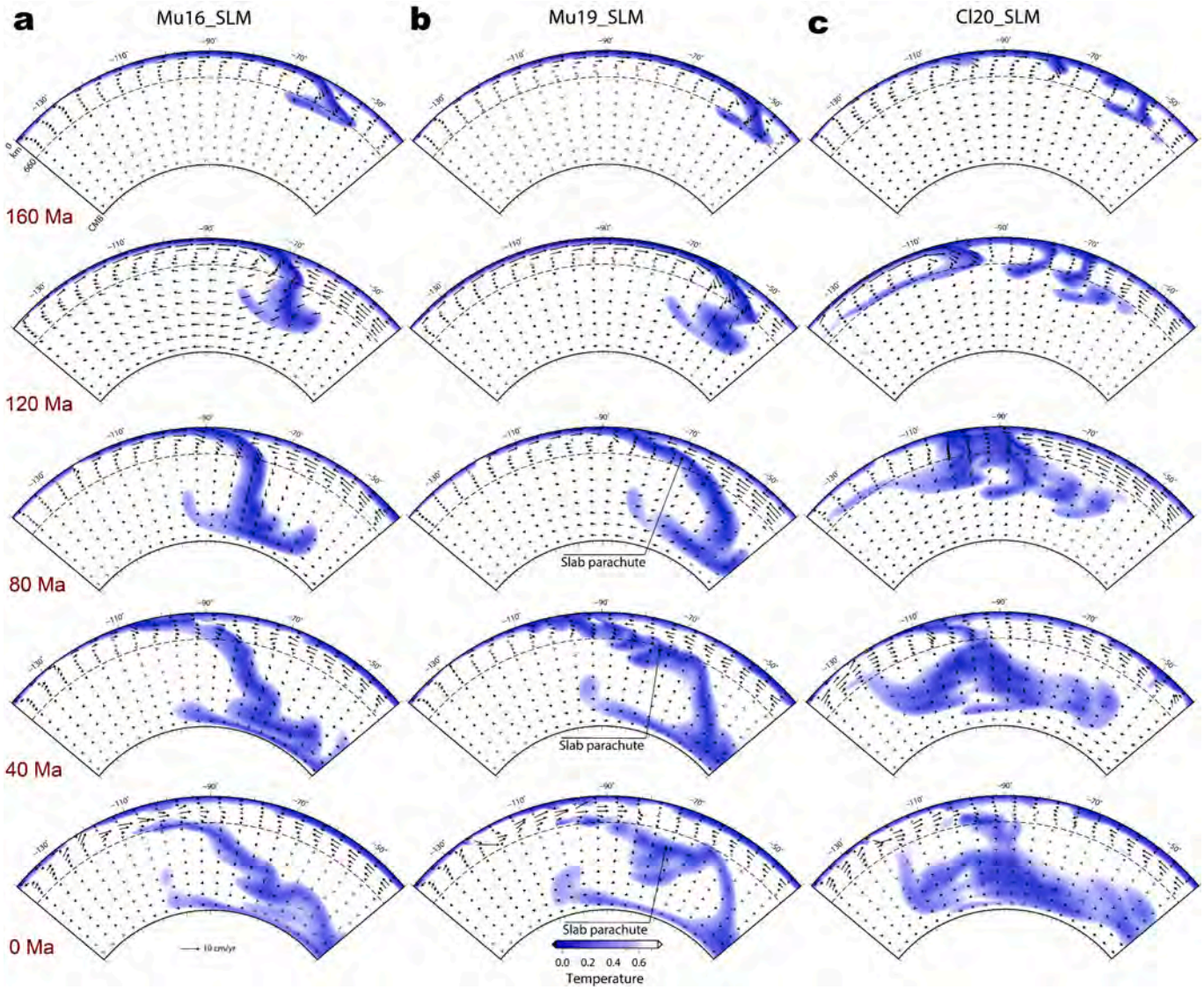

Fig. 9. Simulated subduction histories along 40°N based on the three plate reconstructions. Among these models, Mu16 (a) and Mu19 (b) differ mainly in their trench locations, while Cl20 (c) differs from the other two with multiple intra-oceanic subduction events during the Mesozoic that switched to a single eastward subduction during the Late Cretaceous (e.g., 80 Ma). A movie for the evolution of this cross-section in the three models is available (Movie S2).

Their different amounts of net lithospheric rotation, when projected onto North America, results in faster trench retreat in Mu19 than in Mu16 (Fig. S2, Movie S1). For example, the Farallon trench was ~1000 km more eastward in Mu19 at 160 Ma, and this difference largely disappeared by the latest Cretaceous (Figs. 1, 9). Since this period is prior to the extensional deformation within the western United States, the above Mesozoic difference in trench location is mostly due to the discrepancy in their respective reference frames. Consequently, the simulated Farallon subduction in Mu19 experienced significantly faster trench retreat during the Jurassic-Cretaceous than that in Mu16. As a result, the former model led to a more prominent shallow-to-flat slab beneath western North America during the Mesozoic, consistent with inferences from 2D regional subduction models (Christensen, 1996; van Hunen et al., 2000). In 3D, the center of a subducting slab tends to experience a stronger subslab overpressure that tends to elevate this part of the slab relative to the edges (Liu and Stegman, 2011, 2012). The 3D illustration of the modeled slab more clearly demonstrates this dome-like slab geometry (Fig. 10b). This special slab configuration remained toward the present (Figs. 4,10).

Formation of a broad dome-like slab geometry in Mu19 during the Mesozoic means that this slab 'parachute' will sink more slowly than a steeper and/or shorter slab, because the laterally distributed negative buoyancy of the long slab is more readily balanced by the viscous resistance of the ambient mantle (Stevenson and Turner, 1977; Peng e al., 2021a). Geographically, the center of this slab will sink slower than the edges (Figs. 9, 10). Consequently, the slow sinking of the central Farallon slab in Mu19 during the Cenozoic resulted in a present-day depth that is notably shallower than in Mu16 (Figs. 9a,b, 10) and tomography (Fig. 7). The observation that the northern and southern portions of the Mu19 slab are much deeper than the middle (Fig. 10) further supports the above statement.

The largest difference of Cl20 from Mu16 and Mu19 is that the former hosts multiple intra-oceanic subduction zones within the eastern Pacific during the Mesozoic, when both eastward- and westward-directed subducting slabs developed (Fig. 9c). During the Late Cretaceous (e.g., 80 Ma), these ribboned ocean basins (Fig. 1c,d) were eventually consumed by subduction. Only by this time, eastward Farallon subduction along the west coast of North America commenced, and this subduction lasted to the present. Although the posts-80 Ma subduction of Cl20 is similar as that in Mu16 and Mu19, their different Late-Cretaceous mantle structures caused their subsequent evolution to

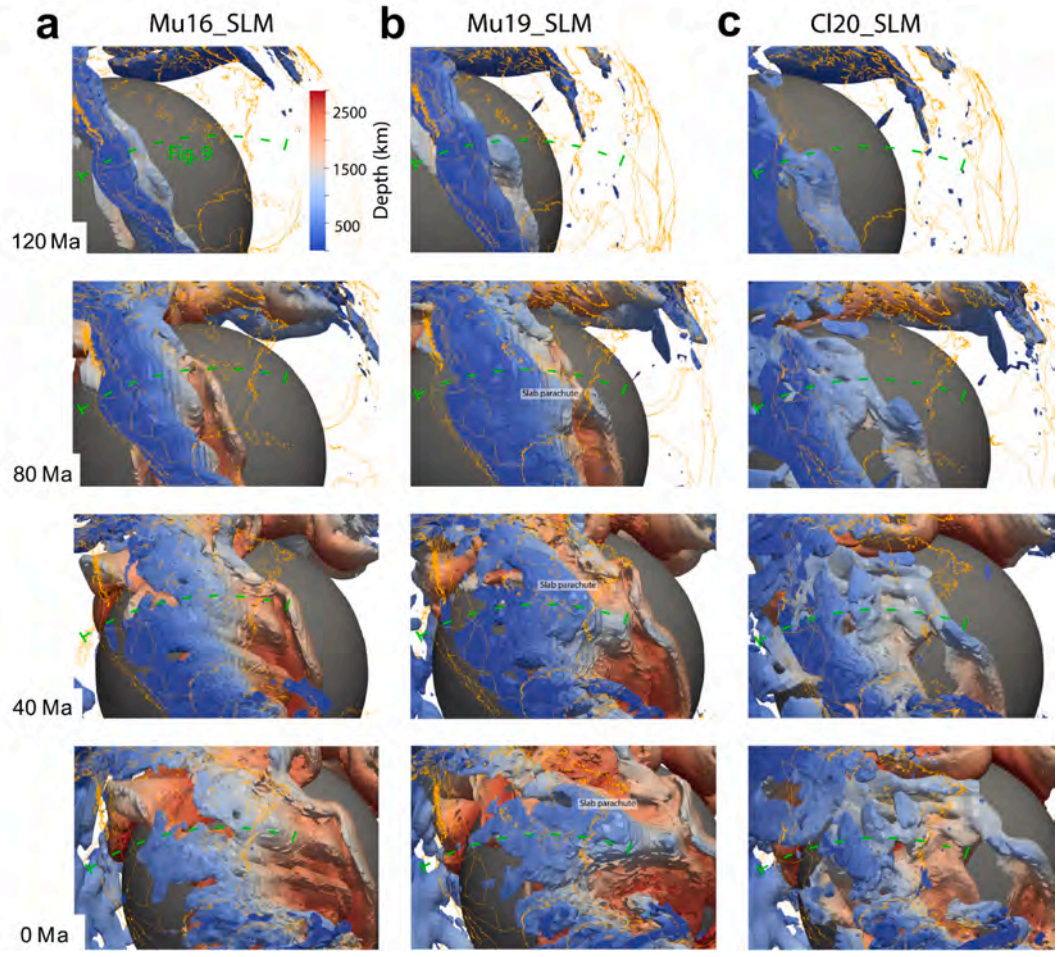

Fig. 10. 3D visualization of evolving slabs below North America. a-c) Models Mu16_SLM, Mu19_SLM, and Cl20_SLM, respectively. Mantle structures below 200 km depth are shown. Slab surfaces correspond to the −150 °C isotherm, with colour showing slab depth. The green dashed line marks the position of Fig. 9. (For interpretation of the references to colour in this figure legend, the reader is referred to the web version of this article.)

differ. In particular, the large volumes of parallel or imbricated slab segments cumulated below the west coast of North America by 80 Ma dominated the Cenozoic sinking trajectory. The downward-to-westward drag of these slabs prohibited the formation a flat slab underneath North America, in contrast to Mu16 and Mu19. The concentrated negative buoyancy also caused the slab pile to sink faster than a thinner single slab. Consequently, the present-day depth of the Cl20 slabs is much greater than that in the other models, as well as than that in the seismic image (Fig. 7).

Both the flat slabs and the shallow slab underplating against the base of the upper plate caused significant deformation within the continental lithosphere, with regional thinning and thickening occurring depending on the stress states. Consequently, the western half of the North American mantle lithosphere was severely reshaped during the Mesozoic (Fig. 9). Since our models acknowledge a layered lithospheric density structure, variations in these layers will modulate surface topography. This topographic contribution is in addition to the so-called dynamic topography induced by the oceanic slab and associated mantle flow (Braun, 2010; Liu, 2015).

3.2.3. *Paleotopography evolution from the three subduction models*

An important independent assessment of the modeled subduction histories is through evaluating the modeled continental topography as a function of time against available geologic constraints (Mitrovica et al., 1989; Gurnis, 1993; Gurnis et al., 1998; Liu et al., 2008; Spasojević et al., 2009; Shephard et al., 2010; Liu and Gurnis, 2010; Heller and Liu, 2016; Liu et al., 2021). Since our models incorporate realistic density structures of the lithosphere based on multiple recent inferences (Hu et al., 2018b; Wang et al., 2022a, 2022b), the resulting topography represents the combined effects from both the evolving lithosphere and the convective mantle underneath. In effect, the results should be directly comparable to that observed, with a caveat that topographic reworkings due to surface processes are absent in these results.

Here we analyze the paleotopography from each of the three models that all have a strong lower mantle (SLM), since the match of slabs with seismic tomography in the WLM cases is not as good (Figs. 6-8). To avoid the influence of the uncertain initial condition, we show the topographic history since the latest Jurassic, when major slabs are well developed. For each time frame, we also remove the globally averaged surface topography, with the purpose of correcting the effect of total mantle buoyancy change due to progressive increase of subducted slab volumes inside an initially empty mantle. Because the initial lithosphere thickness and associated topography of North America are unknown, we choose the present-day model topography as the reference level: we adjust all topography predictions with a constant amount such that the present-day topography of the stable central-eastern continental North America is close to that observed. Finally, we also considered a maximum sea level drop of 200 m from the Late Cretaceous to the present (Müller et al., 2008) in estimating the basement topography of continental North America. The resulting paleo and present topography of North America from the three subduction models are displayed in Fig. 11. For the Mesozoic, we mostly focus on the Cretaceous topography due to the available paleoaltimetry constraints associated with the development of the Western Interior Seaway. We exclude the Cenozoic

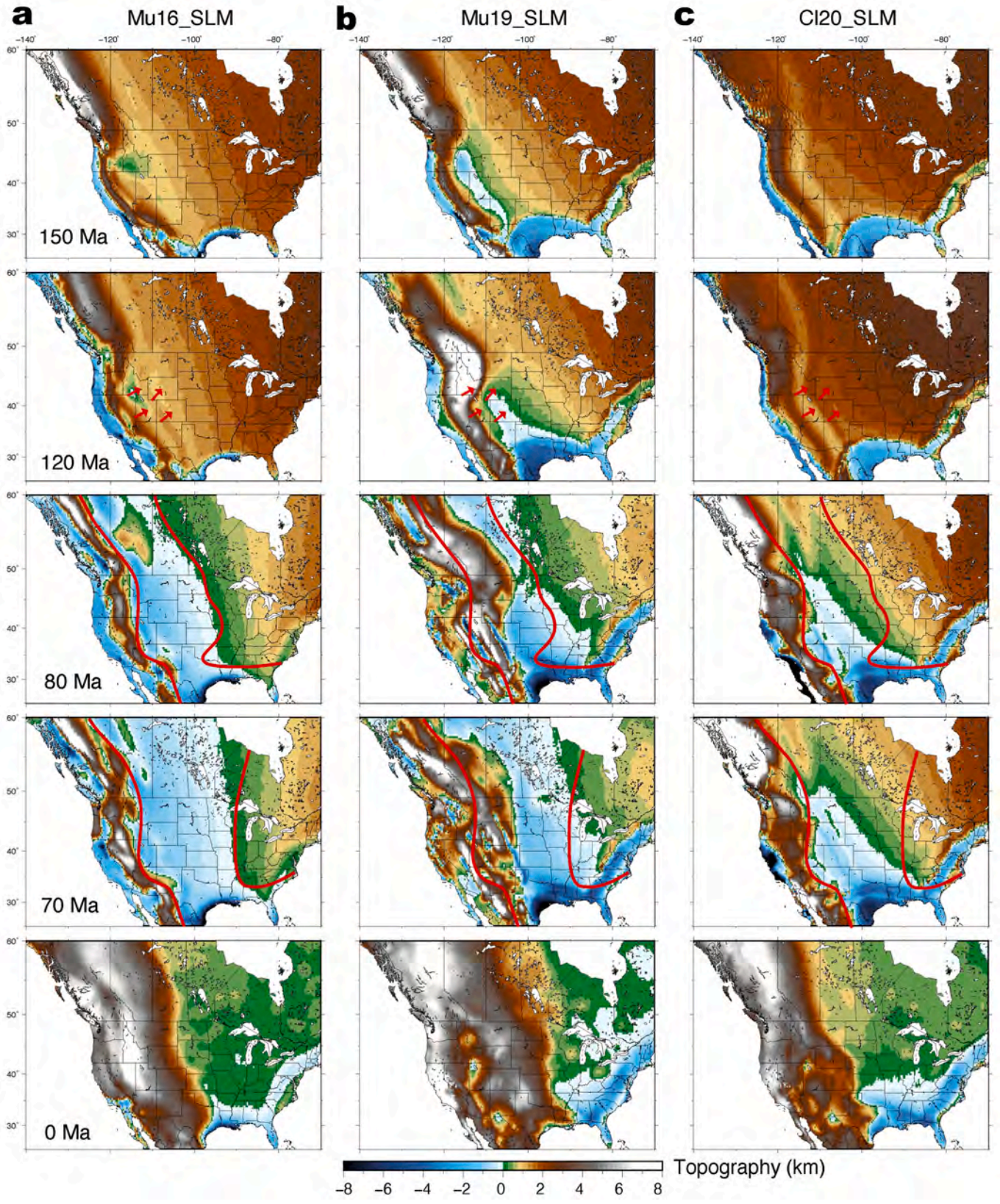

Fig. 11. Paleotopography evolution in North America due to different subduction scenarios. The predicted topographic history assumed a 200-m sea level drop from the Cretaceous to the present. The final (0 Ma) topography of each model is used a reference level such that the eastern North American elevation is adjusted to near the observed topography. Red arrows in 120 Ma represent the area of movement of Early Cretaceous fluvial conglomerate deposits (from Heller et al., 2003). The solid red lines in 80 and 70 Ma represents paleo shorelines of the Cretaceous Interior Seaway, adopted from Heller and Liu (2016) and Liu et al. (2008), respectively. (For interpretation of the references to colour in this figure legend, the reader is referred to the web version of this article.)

part of the history due to both the lack of reliable constraints on paleotopography and the more similar plate kinematics among all three reconstructions than in the Mesozoic (Fig. 1a).

A striking topographic feature is the persistent existence of a Cordillera, mostly reflecting crustal thickening near the subduction zone but lithospheric thinning further inland, along the west coast of North America, whose geometry, width, and altitude varied over time due to different subduction dynamics. This feature appeared as early as the Jurassic in Mu16 and Mu19 (Fig. 11a,b), in response to the active subduction underneath. The Cl20 model did not predict a prominent Cordillera until as late as 100 Ma (not shown) when the eastward Farallon subduction was established (Figs. 1, 11). Due to the lack of surface erosion in these calculations, the Cordilleran topography is likely higher than the real case. In contrast to the west coast, the central-eastern North America experienced great fluctuations in mean elevation over time, from 1 to 2 km in the Jurassic to below sea level in the Late Cretaceous, and to a low-elevation platform at the present. The topographic relief of this part of the continent also changed from being westward downtilting during the Mesozoic to largely flat in the latest Cenozoic. This interior subsidence mostly reflects dynamic topography originating from mantle downwelling.

At the end of Jurassic (150 Ma), most of the continental North America remained high and above sea level, according to all three models. Among them, Mu19 also predicts a broad low land within the western United States, with a narrow seaway occupying the foreland region. This configuration remained largely unchanged into the Early Cretaceous (120 Ma). However, the absence of marine deposition with these ages over Wyoming and Colorado Plateau (DeCelles, 2004) falsifies this prediction. By the Early Cretaceous (120 Ma), the only notable changes occurred in Mu19: the Cordillera significantly expanded and raised its peak elevation in the Pacific Northwest, while the seaway further expanded in the south to cover entire Texas. We interpret the more obvious changes of paleotopography in Mu19 as due to the onset of flat slab subduction (Fig. 9b). The stability of the other two models reflects either the normal ongoing subduction (Fig. 9a) or lack of subduction below the continent (Fig. 9c). When compared to the spatial distribution and flow direction of Early Cretaceous fluvial conglomerate deposits (red arrows in the western U.S., from Heller et al., 2003), the topography of Mu16 represents the most reasonable prediction, while other models violate either the observation of terrestrial setting (Mu19) or surface slope directions (Cl20).

The most dramatic topography variation occurred during the Late Cretaceous, in response to either the full development of the flat Farallon slab (Mu16 and Mu19) or translation of former intra-oceanic slabs underneath the continent due to trench retreat (Cl20). Along the west coast, the enhanced lateral compression caused the orogenic uplift to maintain. On the other hand, the slab underplating also dragged the surface down to below sea level, forming the Cretaceous Western Interior Seaway (WIS). Relative to the spatial extents of the WIS that climaxed at 80–70 Ma, Cl20 clearly underpredicts its spatial extent, due to inadequate dynamic subsidence from the sinking slabs. Mu19, on the contrary, overpredicts the landward limit of the seaway that covered almost the entire eastern United States by 70 Ma. This is consistent with its longest flat and shallow Farallon slab that underplated the entire continent by the latest Cretaceous (Fig. 9b). Another consequence of this flat slab is the overpredicted width of the Cordilleran system whose high topography reached half-way through the WIS, as also violates the stratigraphic records around this time (Liu et al., 2008, 2011; Heller and Liu, 2016; Chang and Liu, 2021). Relatively speaking, Mu16 provides the best matches to both the Cordillera topography and the evolution of the WIS. We note that the rigid North American plate in this reconstruction (Müller et al., 2016) could have caused an underestimate on the width of the orogen west of the seaway, but this seems to be an overall minor effect.

By the present day, all models reproduce the observed *E*-W contrasting topography of North America. The overpredicted Cordilleran topography within the United States in Mu16 is largely due to the omission of Basin & Range extension that would reduce topography in this part significantly (Zhou and Liu, 2019). However, the broad high mountains in western Canada, especially from Mu16 and Mu19, are unrealistic. Among all three models, the Canadian topography is best reproduced in Cl20. This seems to support its associated plate reconstruction where late-Mesozoic eastward subduction directly beneath the Canadian margin is absent (Fig. 1). In contrast, its predicted topography in the United States is more off than other models, in that both the Cordillera and central-eastern continent are too low. In addition, this model also consistently misses the topographic predictions within continental United States during the Mesozoic, as suggests that the plate reconstruction at this latitude range is problematic. However, the respective contributions to topography from absolute plate motions and deformable plate interiors in Mu19 still await more investigation.

4. Implications on the exercise of plate reconstruction

In this study, we systematically evaluate three representative plate reconstructions by examining their implied slab structures, subduction dynamics, and topographic responses. We find that these reconstructions lead to clearly diagnostic differences in these results that could be differentiated using observational constraints. In the retrospect, these evaluations provide useful insight on the input reconstructions of the geodynamic models. Therefore, we propose that the workflow presented in this study represents a tentative approach for better constraining the uncertain aspects of the different plate reconstructions. We do caution that the above analysis is heavily based on data constraints from North America, while those from other parts of the globe are still wanted in future research.

4.1. New constraints on net lithospheric rotation

Both the nature and magnitude of net lithospheric rotation over time remain unclear as the absolute reference frames of these reconstructions are anchored on hotspots that are hypothesized to be deep rooted but whose spatial configuration and movement throughout the mantle remain poorly constrained, say by seismic tomography and hotspot track. As a result, different amounts of net lithospheric rotation remain permissible among different reconstructions. Here we show that net lithospheric rotation can influence subduction dynamics through modulating both trench retreat and mantle flow, and that some slabs (e.g., North America) could discern this global-scale kinematic signal more clearly than others (Fig. 3). By analyzing these slab behaviors, especially the subduction dynamics in the region with high sensitivity (e.g., North America), we arrive at some preliminary understanding on the properties of this net lithosphere rotation.

First, the global analysis at four different subduction zones (Fig. 3) shows that trench retreat is not the only factor controlling slab dynamics. The fact that subduction zones with dramatically different amounts of trench retreat generate very similar slabs at depth, such as in East Asia and South America (Fig. 3a,d) suggests that the horizontal components of mantle flow, either at regional or global scale, must have been reorganized accordingly to result in the similar trajectories and final locations of slabs. This finding is consistent with our recent examination of regional (Peng et al., 2021b) and global (Peng and Liu, 2022, 2023) horizontal mantle flow that demonstrates large geographic discrepancies around the globe. We suggest that the origin and pattern of this spatially varying lateral mantle flow should carry important information about the dynamic interaction of subducting slabs at depth, a topic that deserves more future research.

Second, on a global scale, the modeled slabs in Mu16 provide a statistically better match to the seismic image than M19, with their difference more clearly shown below subduction zones within the eastern Pacific than the western Pacific (Fig. 3). This implies that the reconstruction with a large amount of net lithospheric rotation since the

early Mesozoic is more appropriate in representing the kinematic history of Earth's surface motion. This finding further supports the implicit tomotectonic inference (van der Meer et al., 2010), implying that the required net lithospheric rotation may reflect a global scale lateral motion of the mantle and slabs after subduction, irrespective of whether the slab is continuous with depth or broken. This conclusion is reinforced by the regional analysis within North America, where both the evolving Farallon subduction (Figs. 5-10) and the associated paleotopography (Fig. 11) from Mu16 demonstrate a greater extent of consistency with the observational constraints. The model with minimal net surface rotation (Mu19), in contrast, causes excessive flattening of the Farallon slab that induces enduring and too-to-the-east orogenic uplift and dynamic subsidence during the Mesozoic within continental North America than implied by the geologic records (Fig. 11b). We note again that this inference should and could be reexamined using data from other parts of the world.

4.2. Pros and cons of tomotectonic reconstruction

Through further evaluating the subduction history below North America, we confirm that the explicit tomotectonic reconstructions have a unique merit that is complementary to other reconstructions. For example, permitting intra-oceanic subduction in the northeastern Pacific does help to better reproduce some slab features, such as some mid-mantle fast seismic anomalies below Canada, although this model also predicts more features than seismically imaged (Figs. 4, 8). In addition, the model Cl20 also better predicts the present-day topography in the northern North America (Fig. 11c), although the exact reason and mechanism remains to be further explored. These observations suggest that the earlier exercise of plate reconstruction does need some modification, at least within the Mesozoic northeast Pacific Ocean.

On the other hand, we also find that model Cl20 overall matches both mantle seismic structure and paleotopography the worst among all three models, especially below continental U.S. An important reason lies in the presumption of vertically sinking slabs during the original reconstruction (e.g., Sigloch and Mihalynuk, 2013). As Fig. 3 implies, large-scale horizontal mantle flow should exist that compensates most of the different amounts of trench retreat at the surface in producing similar location of subducted slabs at depth. This flow causes a complex history of lateral displacement of the sinking slabs, as can be seen in the more eastward directed descending motion of the slab in Mu16 than in Mu19, a process that trades off their initial difference of trench locations (Fig. 9). Another intuitive illustration of this complex flow comes from the large mismatches between the predicted slab structure in Cl20 and that in seismic tomography DETOX-P3 (Figs. 6-8), based on which the input plate reconstruction was derived. Here we show that their apparent inconsistency is largely due to the discrepancy between the assumed vertical sinking (Clennett et al., 2020) versus the westward-drifting slab descending trajectories during the Mesozoic (Fig. 9c). Based on the tests done, varying mantle viscosity can mostly affect slab depths and cannot diminish the lateral mismatch (Figs. 6-8).

4.3. Possible improvements in the exercise of plate reconstruction

Based on the observations from this study, we provide some suggestions that future plate reconstruction exercises may consider.

The first note is on the absolute reference frame. Most recent plate reconstructions heavily rely on hotspot tracks in deriving their absolute plate motions. However, the estimates on the relative motions of different hotspots remain variable to debate, as is the case for both paleomagnetic inferences (e.g., Tarduno et al., 2009; Wang et al., 2019; Sun et al., 2021) and numerical simulations (e.g., Steinberger, 2000; O'Neill et al., 2005; Hassan et al., 2016). In view of these existing uncertainties, we further propose that quantitative subduction simulation and geological verification as presented here could represent a unique additional constraint on seeking the correct global reference frame. This could either simply act as a verification for a given plate reconstruction, or they could form a more rigorous iterative workflow through which the reconstruction is progressively adjusted until the numerical model results best match the available seismic and tectonic constraints. With the presented results in this study, we find that the reconstruction of Müller et al. (2016) is most compatible with these additional constraints, although some refinement is still needed, such as that in North America as discussed in section 3. This conclusion may be temporary since similar systematic tests with other major slab systems, such as the Tethys, are not yet done.

Our second suggestion is tailored for improving the exercise of current tomotectonic reconstruction. To better take advantage of the rich information from seismic tomography in constructing past plate kinematics, we suggest the assumption of vertically sinking slabs be dropped. In replacement, the tomographic constraint could be best utilized through a novel iterative workflow following these steps:

i) A sequential global data-assimilation model is performed based on a trial reconstruction. The predicted present-day slab structures are compared with tomography, where their differences constitute a residual field. The associated tectonic responses (e.g., paleotopography) at the surface may contribute directly to computing the residual field or act as an independent check for the final result.
ii) The residual is carried backward to the geological past through an inverse operator such as the adjoint algorithm (e.g., Liu and Gurnis, 2008). The last plate reconstruction is updated accordingly.
iii) Repeat the above procedures until the residual becomes small enough. The final updated plate reconstruction is deemed optimal, which provides the best match to both tectonic and tomographic constraints.

Supplementary data to this article can be found online at https://doi.org/10.1016/j.earscirev.2023.104518.

Declaration of Competing Interest

The authors declare that they have no known competing financial interests or personal relationships that could have appeared to influence the work reported in this paper.

Data availability

Seismic tomography model UU-P07 is available at https://www.atlas-of-the-underworld.org/uu-p07-model/, GyPSuM is available at https://ds.iris.edu/ds/products/emc-gypsum/, GLAD-M25 is available at https://ds.iris.edu/ds/products/emc-glad-m25/, DETOX-P3 is available at https://zenodo.org/record/3993276#.Y-dC53bMK9I. Dataset used in the paper is available at https://zenodo.org/record/7634064#.Y-rryHbMK9K.

Acknowledgement

This work is supported by NSF grant EAR1554554. We also acknowledge the Texas Advanced Computing Center (TACC) for providing an allocation on Frontera. Most figures are prepared with GMT (https://www.generic-mapping-tools.org/) and Paraview (https://www.paraview.org/). Surface velocity and plate boundary files are exported using Gplates (https://www.gplates.org/). The original version of CitcomS is available at www.geodynamics.org/cig/software/citcoms/.

References

Amaru, M.L., 2007. Global travel time tomography with 3-D reference models. Geol. Traiectina Utrecht Univ. 1–174.

Bond, G., 1976. Evidence for continental subsidence in north American during the late cretaceous global submergence. Geology 4, 557–560.

Bower, D.J., Gurnis, M., Flament, N., 2015. Assimilating lithosphere and slab history in 4-D dynamic Earth models. Phys. Earth Planet. Inter. 238, 8–22.

Braun, J., 2010. The many surface expressions of mantle dynamics. Nat. Geosci. 3, 825–833.

Bunge, H.-P., Grand, S.P., 2000. Mesozoic plate- motion history below the Northeast Pacific Ocean from seismic images of the subducted Farallon slab. Nature 405, 337–340.

Burchfiel, B.C., Cowan, D.S., Davis, G.A., 1992. Tectonic overview of the Cordilleran orogenin the western United States, in The Cordilleran Orogen: Conterminous U.S., G- 3. In: Burchfiel, B.C. (Ed.). Geol. Soc. of Am., The geology of North America, Boulder, Colo, pp. 407–479.

Butterworth, N.P., Talsma, A.S., Müller, R.D., Seton, M., Bunge, H.P., et al., 2014. Geological, tomographic, kinematic and geodynamic constraints on the dynamics of sinking slabs. J. Geodyn. 73, 1–13.

Chang, C., Liu, L., 2021. Investigating the formation of Cretaceous Western Interior Seaway using landscape evolution simulations. GSA Bull. 133 (1–2), 347–361.

Christensen, U.R., 1996. The influence of trench migration on slab penetration into the lower mantle. Earth Planet. Sci. Lett. 140, 27–39.

Clennett, E.J., Sigloch, K., Mihalynuk, M.G., Seton, M., Henderson, M.A., Hosseini, K., et al., 2020. A quantitative tomotectonic plate reconstruction of western North America and the eastern Pacific basin. Geochem. Geophys. Geosyst. 20, e2020GC009117.

Clift, P.D., Draut, A.E., Kelemen, P.B., Bluszatajn, J., Greene, A., 2005. Stratigraphic and geochemical evolution of an oceanic arc upper crustal section: the Jurassic Talkeetna Volcanic Formation, south-Central Alaska. Geol. Soc. Am. Bull. 117, 902–925.

Coney, P.J., Jones, D.L., Monger, J.W.H., 1980. Cordilleran suspect terranes. Nature 288, 329–333.

Coney, P.J., Reynolds, S.J., 1977. Cordilleran Benioff zones. Nature 270, 403–406.

DeCelles, P.G., 2004. Late Jurassic to Eocene evolution of the Cordilleran thrust belt and foreland basin system, western USA. Am. J. Sci. 304, 105–168.

Domeier, M., Doubrovine, P.V., Torsvik, T.H., Spakman, W., Bull, A.L., 2016. Global correlation of lower mantle structure and past subduction. Geophys. Res. Lett. 43, 4945–4953.

Domeier, M., Shephard, G.E., Jakob, G.E., Gaina, C., Doubrovine, P.V., Torsvik, T.H., 2017. Intraoceanic subduction spanned the Pacific in the Late Cretaceous–Paleocene. Science Advances 3 (11), eaao2303.

Engebretson, D.C., Cox, A., Gordon, R.G., 1985. Relative motions between oceanic and continental plates in the Pacific basin, 206. Geological Society of America. Special Paper.

French, S.W., Romanowicz, B.A., 2014. Whole-mantle radially anisotropic shear velocity structure from spectral-element waveform tomography. Geophys. J. Int. 199 (3), 1303–1327.

Gerya, T.V., Bercovici, D., Becker, T.W., 2021. Dynamic slab segmentation due to brittle–ductile damage in the outer rise. Nature 559, 245–250.

Gurnis, M., 1993. Phanerozoic marine inundation of continents driven by dynamic topography above subducting slabs. Nature 364, 589–593.

Gurnis, M., Müller, R.D., Moresi, L., 1998. Dynamics of cretaceous vertical motion of Australia and the Australian-Antarctic discordance. Science 279, 1499–1504.

Hassan, R., Müller, R.D., Gurnis, M., Williams, S.E., Flament, N., 2016. A rapid burst in hotspot motion through the interaction of tectonics and deep mantle flow. Nature 533, 239–242.

Heller, P.L., Dueker, K., McMillan, M.E., 2003. Post-Paleozoic alluvial gravel transport as evidence of continental tilting in the U.S. Cordillera. GSA Bull. 115, 1122–1132.

Heller, P., Liu, L., 2016. Dynamic topography and vertical motion of the U.S. Rocky Mountain region prior to and during the Laramide orogeny. GSA Bull. 128, 973–988.

Hosseini, K., Sigloch, K., Tsekhmistrenko, M., Zaheri, A., Nissen-Meyer, T., Igel, H., 2020. Global mantle structure from multifrequency tomography using P, PP and P-diffracted waves. Geophys. J. Int. 220, 96–141.

Hosseinpour, M., Williams, S., Seton, M., Barnett-Moore, N., Müller, R.D., 2016. Tectonic evolution of Western Tethys from Jurassic topresent day: Coupling geological and geophysical data with seismic tomography models. Int. Geol. Rev. 6814, 1–30. https://doi.org/10.1080/00206814.2016.118314.

Hu, J., Liu, L., Hermosillo, A., Zhou, Q., 2016. Simulation of late Cenozoic South American Flat-Slab Subduction using Geodynamic Models with Data Assimilation. Earth Planet. Sci. Lett. 438, 1–13.

Hu, J., Liu, L., Zhou, Q., 2018. Reproducing past subduction and mantle flow using high-resolution global convection models. Earth Planet. Phys. 2, 1–18.

Hu, J., Liu, L., Faccenda, M., Zhou, Q., Fischer, K.M., Marshak, S., Lundstrom, C., 2018b. Modification of the Western Gondwana craton by plume–lithosphere interaction. Nat. Geosci. 11 (3), 203–210.

Lei, W., Ruan, Y., Bozdağ, E., Peter, D., Lefebvre, M., Komatitsch, D., Tromp, J., Hill, J., Podhorszki, N., Pugmire, D., 2020. Global adjoint tomography—model GLAD-M25. Geophys. J. Int. 223, 1–21.

Li, C., van der Hilst, R.D., Engdahl, E.R., Burdick, S., 2008. A new global model for P wave speed variations in Earth's mantle. Geochem. Geophys. Geosyst. 9 (5).

Li, Z., Aschoff, J., 2022. Shoreline evolution in the late cretaceous north American Cordilleran foreland basin: an exemplar of the combined influence of tectonics, sea level, and sediment supply through time. Earth Sci. Rev. 226, 103947.

Lin, Y.-A., Colli, L., Wu, J., 2022. NW Pacific-Panthalassa intra-oceanic subduction during Mesozoic times from mantle convection and geoid models. Geochem. Geophys. Geosyst. e2022GC010514.

Liu, L., 2012. Lost sea floor. Nat. Geosci. 5, 165–167.

Liu, L., 2015. The Ups and Downs of North America: evaluating the Role of Mantle Dynamic Topography since the Mesozoic. Rev. Geophys. 53 https://doi.org/10.1002/2015RG000489.

Liu, L., Gurnis, M., 2008. Simultaneous Inversion of Mantle Properties and initial Conditions using an Adjoint of Mantle Convection. J. Geophys. Res. Solid Earth 113, B08405.

Liu, L., Gurnis, M., 2010. Dynamic subsidence and uplift of the Colorado Plateau. Geology 38 (7), 663–666.

Liu, L., Spasojević, S., Gurnis, M., 2008. Reconstructing Farallon Plate Subduction beneath North America back to the late cretaceous. Science 322, 934–938.

Liu, L., Stegman, D.R., 2011. Segmentation of Farallon slab. Earth Planet. Sci. Lett. 311, 1–10.

Liu, L., Stegman, D.R., 2012. Origin of Columbia River flood basalt controlled by propagating rupture of the Farallon slab. Nature 482, 386–389.

Liu, L.D., Peng, L., Liu, L., Chen, S., Li, Y., Wang, Z.Cao, Feng, M., 2021. East asian lithospheric evolution dictated by multistage Mesozoic flat-slab subduction. Earth Sci. Rev. 217, 103621.

Liu, S., Nummedal, D., Liu, L., 2011. Tracking the Farallon plate migration through the Late Cretaceous Western U.S. Interior Basins. Geology 39, 555–558.

Liu, Y., Liu, L., Li, Y., Peng, D., Wu, Z., Cao, Z., Li, S., Du, Q., 2022. Global back-arc extension due to trench-parallel mid-ocean ridge subduction. Earth Planet. Sci. Lett. 600, 117889.

Liu, L., Zhou, Q., 2015. Deep recycling of oceanic asthenosphere material during subduction. Geophys. Res. Lett. 42 (7), 2204–2211.

Ma, P., Liu, S., Gurnis, M., Zhang, B., 2019. Slab horizontal subduction and slab tearing beneath East Asia. Geophys. Res. Lett. 46 (10), 5161–5169.

Mao, W., Zhong, S., 2018. Slab stagnation due to a reduced viscosity layer beneath the mantle transition zone. Nat. Geosci. 11 (11), 876–881.

Mitrovica, J.X., Beaumont, C., Jarvis, G.T., 1989. Tilting of continental interiors by the dynamical effects of subduction. Tectonics 8, 1079–1094.

Müller, R.D., Royer, J.-Y., Lawver, L.A., 1993. Revised plate motions relative to the hotspots from combined Atlantic and Indian Ocean hotspot tracks. Geology 21 (3), 275–278.

Müller, R.D., Sdrolias, M., Gaina, C., Steinberger, B., Heine, C., 2008. Long-term sea-level fluctuations driven by ocean basin dynamics. Science 319, 1357–1362.

Müller, R.D., Seton, M., Zahirovic, S., Williams, S.E., Matthews, K.J., Wright, N.M., et al., 2016. Ocean Basin Evolution and Global-Scale Plate Reorganization events since Pangea Breakup. Annu. Rev. Earth Planet. Sci. 44 (1), 107–138.

Müller, R.D., Zahirovic, S., Williams, S.E., Cannon, J., Seton, M., Bower, D.J., et al., 2019. A global plate model including lithospheric deformation along major rifts and orogens since the Triassic. Tectonics 38, 1884–1907.

Obayashi, M., Yoshimitsu, J., Nolet, G., Fukao, Y., Shiobara, H., Sugioka, H., et al., 2013. Finite frequency whole mantle P wave tomography: Improvement of subducted slab images. Geophys. Res. Lett. 40 (21), 5652–5657.

O'Neill, C., Müller, R.D., Steinberger, B., 2005. On the uncertainties in hotspot reconstructions, and the significance of moving hotspot reference frames. Geochem. Geophys. Geosyst. 6, Q04003.

Pavlis, T.L., Amato, J.M., Trop, J.M., Ridgway, K.D., Roeske, S.M., Gehrels, G.E., 2019. Subduction Polarity in Ancient Arcs: a call to Integrate Geology and Geophysics to Decipher the Mesozoic Tectonic history of the Northern Cordillera of North America. GSA Today 29.

Peng, D., Liu, L., Wang, Y., 2021a. A newly discovered Late-cretaceous East asian flat slab explains its unique lithospheric structure and tectonics. J. Geophys. Res. Solid Earth 126, e2021JB022103.

Peng, D., Liu, L., Hu, J., Li, S., Liu, Y., 2021b. Formation of East asian stagnant slabs due to a pressure-driven Cenozoic mantle wind following Mesozoic subduction. Geophys. Res. Lett. 48, e2021GL094638.

Peng, D., Liu, L., 2022. Quantifying slab sinking rates using global geodynamic models with data-assimilation. Earth Sci. Rev. 104039.

Peng, D., Liu, L., 2023. Importance of global spherical geometry for studying slab dynamics and evolution in models with data assimilation. Earth Sci. Rev. 241, 104414.

Ritsema, J., Deuss, A., Van Heijst, H.J., Woodhouse, J.H., 2011. S40RTS: a degree-40 shear-velocity model for the mantle from new Rayleigh wave dispersion, teleseismic traveltime and normal-mode splitting function measurements. Geophys. J. Int. 184 (3), 1223–1236.

Saleeby, J., 2003. Segmentation of the Laramide slab — evidence from the southern Sierra Nevada region. Geol. Soc. Am. Bull. 115, 655–668.

Schellart, W.P., Freeman, J., Stegman, D.R., Moresi, L., May, D.A., 2007. Evolution and diversity of subduction zones controlled by slab width. Nature 446, 308–311.

Schuberth, B.S.A., Bunge, H.P., Steinle-Neumann, G., Moder, C., Oeser, J., 2009. Thermal versus elastic heterogeneity in high-resolution mantle circulation models with pyrolite composition: High plume excess temperatures in the lowermost mantle. Geochem. Geophys. Geosyst. 10, Q01W01.

Seton, M., Müller, R.D., Zahirovic, S., Gaina, C., Torsvik, T.H., Talsma, A.G., et al., 2012. Global continental and ocean basin reconstructions since 200 Ma. Earth Sci. Rev. 113 (3–4), 212–270.

Shephard, G.E., Müller, R.D., Liu, L., Gurnis, M., 2010. Miocene Amazon River drainage reversal caused by plate-mantle dynamics. Nat. Geosci. 3, 870–875.

Sigloch, K., 2011. Mantle provinces under North America from multifrequency P wave tomography. Geochem. Geophys. Geosyst. 12. Q02W08.

Sigloch, K., Mihalynuk, M.G., 2013. Intra-oceanic subduction shaped the assembly of Cordilleran North America. Nature 496, 50–56.
Simmons, N.A., Forte, A.M., Boschi, L., Grand, S.P., 2010. GyPSuM: a joint tomographic model of mantle density and seismic wave speeds. J. Geophys. Res. Solid Earth 115, B12310.
Spasojević, S., Liu, L., Gurnis, M., 2009. Adjoint Convection Models of North America Incorporating Tomographic, Plate motion and Stratigraphic Constraints. Geochem. Geophys. Geosyst. 10, Q05W02.
Sun, W., Langmuir, C.H., Ribe, N.M., Zhang, L., Sun, S., Li, H., Li, C., Fan, W., Tackley, P. J., Sanan, P., 2021. Plume-ridge interaction induced migration of the Hawaiian-Emperor seamounts. Sci. Bull. 66, 1691–1697.
Stadler, G., Gurnis, M., Burstedde, C., Wilcox, L.C., Alisic, L., Ghattas, O., 2010. The dynamics of plate tectonics and mantle flow: from local to global scales. Science 329, 1033–1038.
Steinberger, B., 2000. Plumes in a convecting mantle: Models and observations for individual hotspots. J. Geophys. Res. Solid Earth 105, 11127–11152.
Steinberger, B., Torsvik, T., 2008. Absolute plate motions and true polar wander in the absence of hotspot tracks. Nature 452, 620–623.
Steinberger, B., Torsvik, T.H., Becker, T.W., 2012. Subduction to the lower mantle – a comparison between geodynamic and tomographic models. Solid Earth 3, 415–432.
Stevenson, D.J., Turner, J.S., 1977. Angle of subduction. Nature 270, 334–336.
Tan, E., Choi, E., Thoutireddy, P., Gurnis, M., Aivazis, M., 2006. GeoFramework: coupling multiple models of mantle convection within a computational framework. Geochem. Geophys. Geosyst. 7, 1–14.
Tarduno, J., Bunge, H.-P., Sleep, N., Hansen, 2009. U. The bent Hawaiian-Emperor hotspot track: inheriting the mantle wind. Science 324, 50–53.
Torsvik, T.H., Müller, R.D., Van der Voo, R., Steinberger, B., Gaina, C., 2008. Global plate motion frames: toward a unified model. Rev. Geophys. 46, RG3004.
Torsvik, T.H., Steinberger, B., Shephard, G.E., Doubrovine, P.V., Gaina, C., Domeier, M., et al., 2019. Pacific-Panthalassic reconstructions: Overview, errata and the way forward. Geochem. Geophys. Geosyst. 20, 3659–3689.
van der Meer, D.G., Spakman, W., van Hinsbergen, D.J.J., Amaru, M.L., Torsvik, T.H., 2010. Towards absolute plate motions constrained by lower-mantle slab remnants. Nat. Geosci. 3, 36–40.
van der Meer, D.G., Torsvik, T.H., Spakman, W., van Hinsbergen, D.J.J., Amaru, M.L., 2012. Intra-Panthalassa Ocean subduction zones revealed by fossil arcs and mantle structure. Nat. Geosci. 5, 215–219.
van der Meer, D.G., van Hinsbergen, D.J.J., Spakman, W., 2018. Atlas of the underworld: Slab remnants in the mantle, their sinking history, and a new outlook on lower mantle viscosity. Tectonophysics 723, 309–448.
van Hunen, J., van den Berg, A.P., Vlaar, N.J., 2000. A thermo-mechanical model of horizontal subduction below an overriding plate. Earth Planet. Sci. Lett. 182, 157–169.
Wang, C., Gordon, R.G., Zhang, T., Zheng, L., 2019. Observational test of the global moving hot spot reference frame. Geophys. Res. Lett. 46, 8031–8038.
Wang, Y., Liu, L., Zhou, Q., 2022a. Topography and gravity reveal denser cratonic lithospheric mantle than previously thought. Geophys. Res. Lett. e2021GL096844.
Wang, Y., Liu, L., Zhou, Q., 2022b. Geoid reveals the Density Structure of Cratonic Lithosphere. J. Geophys. Res. Solid Earth 127, e2022JB024270.
Wu, J., Suppe, J., Lu, R., Kanda, R., 2016. Philippine Sea and East asian plate tectonics since 52 Ma constrained by new subducted slab reconstruction methods. J. Geophys. Res. Solid Earth 121, 4670–4741.
Zahirovic, S., Matthews, K.J., Flament, N., Müller, R.D., Hill, K.C., Seton, M., et al., 2016. Tectonic evolution and deep mantle structure of the eastern Tethys since the latest Jurassic. Earth-Sci. Rev. 162, 293–337.
Zhong, S., McNamara, A., Tan, E., Moresi, L., Gurnis, M., 2008. A benchmark study on mantle convection in a 3-D spherical shell using CitcomS. Geochem. Geophys. Geosyst. 9, Q10017.
Zhou, Q., Liu, L., Hu, J., 2018. Origin of Yellowstone Volcanic Province due to Intruding Hot Mantle Driven by Ancient Farallon Slab. Nature Geosci. 11, 70–77.
Zhou, Q., Liu, L., 2019. Topographic evolution of the western United States since the early Miocene. Earth Planet. Sci. Lett. 514, 1–12.